



## Evaluation of MSG-SEVIRI mineral dust retrieval products over North Africa and the Middle East

J.R. Banks\*, H.E. Brindley

*Space and Atmospheric Physics Group, Imperial College, London, UK*

### ARTICLE INFO

#### Article history:

Received 16 April 2012

Received in revised form 17 July 2012

Accepted 21 July 2012

Available online 30 October 2012

#### Keywords:

Geostationary satellite observations

Infrared remote sensing of dust

Aerosol optical depth

### ABSTRACT

High temporal resolution observations from the Spinning Enhanced Visible and InfraRed Imager (SEVIRI), on the Meteosat Second Generation satellites, can offer new insights into the processes governing the behaviour of dust sources. Here we evaluate a multi-year, high time-resolution record of dust flagging and dust aerosol optical depth (DAOD) derived from SEVIRI to identify diurnal patterns of dust loading, and diagnose issues with the dust retrievals over North Africa and Arabia. The original dust detection scheme falsely flags dust in regions of high 8.7 μm emissivity. The implementation of an updated scheme mitigates this by making use of the mean 10.8–8.7 μm brightness temperature difference in order to isolate airborne dust from rocky surfaces. Comparing the DAODs (at 550 nm) retrieved using the different schemes with co-located AERONET observations, the impact is relatively small (RMS < 0.02); however, these sites tend to be situated away from the regions where false detections are prevalent. For these regions, the application of the new scheme tends to provide a more consistent DAOD baseline for when the dust flag is triggered, important for the creation of a consistent data record. Turning to the DAODs themselves, RMS differences with the AERONET sites range from 0.19 to 0.46, but show a clear seasonal variation in the level of agreement, with higher biases in the boreal winter.

© 2012 Elsevier Inc. All rights reserved.

### 1. Introduction

One of the most significant sources of uncertainty in our understanding of climate change is the role played by aerosols (Forster et al., 2007). Mineral dust is one of the dominant species of aerosol in the global climate system, comprising as much as 40% of the global aerosol burden by mass according to model estimates (Stier et al., 2005). The Sahara desert in North Africa is by far the largest source of mineral dust, contributing as much as 65% of global dust emissions (Ginoux et al., 2004), with potential impacts on human health (Goudie & Middleton, 2006) and marine biogeochemistry in neighbouring seas and oceans (Guerzoni et al., 1997; Jickells et al., 2005), as well as having a major impact on the radiation budget (e.g. Hsu et al., 2000).

Satellites can provide extensive observations of dust and can help to identify dust sources (e.g. Ginoux et al., 2010; Prospero et al., 2002; Schepanski et al., 2007; Washington et al., 2003) and quantify the dust radiative impacts (e.g. Brindley, 2007; Slingo et al., 2006). Dust detection methods have been developed for various satellite instruments in low Earth orbit such as the MODerate resolution Imaging Spectroradiometer (MODIS) and the Multi-angle Imaging SpectroRadiometer (MISR), both

operated by NASA (Martonchik et al., 2004; Miller, 2003). Observations from the Spinning Enhanced Visible and InfraRed Imager (SEVIRI) instrument on the geostationary Meteosat Second Generation (MSG) satellites (Schmetz et al., 2002) provide data and imagery across Africa at a high temporal resolution of every 15 minutes, and a horizontal resolution at nadir of ~3 km. These observations give unparalleled temporal and spatial coverage of dust activity over the Sahara and the Middle East, enabling the observation of the life-cycle of dust storms in these regions. Measurements from SEVIRI can be used to identify atmospheric dust, and to infer the dust aerosol optical depth (Brindley & Russell, 2009), hereafter BR09.

In this paper we seek to evaluate the performance of the BR09 approach, over a three-year period (2008–2010). This extends (both seasonally and annually) the period covered by BR09, who evaluated DAOD from SEVIRI for March–August in 2006. Through knowledge of the surface emissivity, albedo and temperature, and the solar zenith angle, we can understand the strengths and weaknesses of the dust detection algorithm. Hence we propose improvements to the dust detection algorithm by screening out pixels falsely flagged as dust due to the surface spectral properties. We assess the impact on the output dust flags and DAODs and illustrate the relationship between them, indicating what dust loading is required to trigger a dust detection and why this is important. We use the Aerosol Robotic Network (AERONET) of sun-photometers (Holben et al., 1998) for ground-truthing of the resultant DAOD values to assess the performance of the retrieval scheme over different areas on seasonal and annual timescales.

\* Corresponding author at: Space and Atmospheric Physics Group, The Blackett Laboratory, Imperial College London, Prince Consort Road, London, SW7 2BW, UK.  
Tel.: +44 207 5947677; fax: +44 207 7594 7772.

E-mail address: [j.banks@imperial.ac.uk](mailto:j.banks@imperial.ac.uk) (J.R. Banks).

## 2. SEVIRI dust visualisation and quantification methods

### 2.1. SEVIRI

SEVIRI, located on the Meteosat Second Generation series of satellites operated by the European Organisation for the Exploitation of Meteorological Satellites (EUMETSAT), has eleven spectral channels in the visible and the infrared ( $0.6, 0.8, 1.6, 3.9, 6.2, 7.3, 8.7, 9.7, 10.8, 12.0$ , and  $13.4\text{ }\mu\text{m}$ ) at a nadir spatial resolution of  $3\text{ km}$ , and an extra high-resolution visible channel at a nadir resolution of  $1\text{ km}$  (Schmetz et al., 2002). To measure broadband radiation, MSG also carries the Geostationary Earth Radiation Budget (GERB) instrument (Harries et al., 2005). The data from SEVIRI and GERB used in this study have been provided by the Royal Meteorological Institute of Belgium (RMIB).

SEVIRI raw data is defined in terms of counts. In order to extract the radiance  $B$  ( $\text{mW m}^{-2}\text{ sr}^{-1}(\text{cm}^{-1})^{-1}$ ), the offset and the gain are required (Lensky & Rosenfeld, 2008):

$$B = \text{offset} + (\text{gain} \times \text{count}). \quad (1)$$

The offsets and gains are defined individually for each channel. To calculate the brightness temperature  $T_B$  (K) we invert the Planck function:

$$T_B = \left( \frac{c_2\nu}{\ln^{c_1\nu^3} + 1} - b \right) / a, \quad (2)$$

where  $\nu$  is the central wavenumber of the channel ( $\text{cm}^{-1}$ ) and the coefficients have values  $c_1 = 1.19104 \times 10^{-5}\text{ mW m}^{-2}\text{ sr}^{-1}(\text{cm}^{-1})^{-4}$  and  $c_2 = 1.43877\text{ K}(\text{cm}^{-1})^{-1}$ . The assumed values of coefficients  $a$  and  $b$  at the relevant wavelengths are listed in Table 1, which arise from the definition of the radiance as the effective radiance (Lensky & Rosenfeld, 2008). This is a correction to account for the width of the spectral response function for each channel; before May 2008, the data were defined as the spectral radiance, which did not include the coefficients  $a$  and  $b$ . The reflectance channels  $R_{006}$  and  $R_{016}$  are obtained by dividing the radiance by the product of the cosine of the solar zenith angle and the extraterrestrial solar flux, assuming Lambertian reflection.

### 2.2. 'Desert Dust' RGB imagery

A widely employed imaging technique which aims to isolate airborne dust using SEVIRI is described in detail by Lensky and Rosenfeld (2008). The channel combinations that make up this colour scheme are defined in Table 2. In this scheme mineral dust generally appears to be very pink (hence it is also known as 'pink-dust'), a result of the high contrast between the  $T_{B120}$  and the  $T_{B108}$  channels (red), moderate values of  $T_{B108}$  (moderate blue), and the high emissivity of small quartz dust particles in the  $8.7\text{ }\mu\text{m}$  channel leading to a low contrast between the  $T_{B108}$  and the  $T_{B087}$  channels (low green). By comparison, during the daytime the sandy desert surface appears white or light blue, a consequence of high  $T_{B108}$  and low  $T_{B087}$  since the  $8.7\text{ }\mu\text{m}$  emissivity of large surface quartz particles is small. Note that the assumption that dust is pure quartz is an idealised case. For example, dust originating from the Sahel and Sahara during the GERBILS campaign (Haywood et

**Table 2**  
Combination of channels comprising the 'desert dust' RGB imagery.

Beam	Red	Green	Blue
Channel	$T_{B120} - T_{B108}$	$T_{B108} - T_{B087}$	$T_{B108}$
Min (K)	-4	0	261
Max (K)	2	15	289
Stretch	1	2.5	1

al., 2011) was shown to be predominantly composed of clay minerals (Klaver et al., 2011) which will change the 'colour' of the dust in the 'pink-dust' imagery. Thick cloud appears to be red, while clouds at varying altitudes can also appear green or purple. Rocky desert surfaces such as mountains or hamadas, which are flat and have a stony surface (Mabbutt, 1977), can appear to be purple due to their high emissivity in the  $8.7\text{ }\mu\text{m}$  channel, causing potential confusion with airborne dust.

This imaging technique is an excellent tool as a visual aid for identifying the presence of dust plumes, but it is difficult to use quantitatively. Its usefulness is also impaired at night when the values of  $T_{B108}$  drop, causing the background values of the red beam to dominate, so losing contrast between the background desert and the airborne dust. Recent observations from the Fennec campaign in June 2011 suggest that  $\sim 50\%$  of dust uplift is nocturnal (Marsham et al., submitted for publication), which may be missed in the imagery. Moreover, at weak dust loadings the imagery does not produce a noticeable pink signal, so it can be difficult to visually identify such dust loadings. High column water vapour may also mask the presence of dust (Brindley et al., 2012). For a more objective analysis of dust activity, dust detection methods which use selected wavelength channel combinations and fixed thresholds may be used instead.

### 2.3. Dust detection

Dust detection is calculated using the methodology provided by the EUMETSAT Satellite Application Facilities center for Nowcasting (MétéoFrance, 2011). As with the 'desert dust' imagery, the basis of the dust detection method is the difference between various thermal channels, although some of the criteria use reflectance channels for finer discrimination. Due to the high atmospheric transmission in the  $10.8\text{ }\mu\text{m}$  channel, this channel is generally used as the reference channel, being the most indicative of the apparent surface temperature under clear conditions. By comparing the  $3.9$ , the  $8.7$ , and the  $12.0\text{ }\mu\text{m}$  channels against the  $10.8\text{ }\mu\text{m}$  channel, the effects of varying surface temperatures on the discrimination of dust in the atmosphere can be mitigated. This is also the channel whose brightness temperature is most reduced in the presence of dust aerosol (Merchant et al., 2006). In evaluating the dust detection and DAOD schemes, we focus on North Africa and the Middle East, a domain stretching from  $25^\circ\text{W}$  to  $65^\circ\text{E}$ , and from  $0$  to  $50^\circ\text{N}$ . The scheme is designed for high solar elevation and is most accurate for non-limb views, so detections are only carried out where the solar and viewing zenith angles are less than  $70^\circ$ . Based on these conditions, we carry out detections half-hourly from 0600 to 1600 UT each day.

The first pair of criteria (Eqs. (3) and (4)) are based on the work of Ackerman (1989), who found that the minimum brightness temperature difference between a near and a mid-infrared channel over a turbid dusty desert atmosphere was  $-10\text{ K}$  at night, and  $12\text{ K}$  during the day. In the context of SEVIRI, this is recast as the difference between the  $3.9$  and the  $10.8\text{ }\mu\text{m}$  channels, and the criteria are defined by the following equations (MétéoFrance, 2011):

$$\begin{aligned} T_{B039} - T_{B108} &> -10\text{ K} \text{ and} \\ T_{B120} - T_{B108} &> 2.5\text{ K}, \end{aligned} \quad (3)$$

and

$$\begin{aligned} T_{B039} - T_{B108} &> 12\text{ K} \text{ and} \\ T_{B120} - T_{B108} &> 0.6\text{ K}. \end{aligned} \quad (4)$$

**Table 1**

SEVIRI Planck function coefficients of relevant channels for MSG1, as provided by (Lensky & Rosenfeld, 2008).

Channel	Wavelength ( $\mu\text{m}$ )	$a$	$b$ (K)
4	3.9	0.9959	3.471
7	8.7	0.9996	0.181
9	10.8	0.9983	0.627
10	12.0	0.9988	0.397
11	13.4	0.9981	0.576

During the daytime there will also be a solar reflectance component to the 3.9 μm channel, as well as the thermal component. This adds to the complexity of the dust detection scheme, and it is due to this that the threshold is set to 12 K during the day when the reflectance component to the radiance signal in the 3.9 μm channel is strongest (Ackerman, 1989). The difference between the  $T_{B120}$  and the  $T_{B108}$  channels is included in order to discriminate dust plumes from water/ice clouds (Prata, 1989): the difference is generally positive for mineral dust. Note that as the moisture content of the air increases  $T_{B120}$  will be depressed faster than  $T_{B108}$ , so the signal for the dust detection may be inhibited (Brindley et al., 2012).

The second pair of criteria (Eqs. (5) and (6)) are based on the difference in emissivity in the 8.7 μm channel between lofted small dust particles and large dust particles on the desert surface (Lensky & Rosenfeld, 2008). Again, the  $T_{B120}$  channel is used to isolate and remove water/ice clouds from the dust detection, hence the relevant equations are (MétéoFrance, 2011):

$$\begin{aligned} T_{B120} - T_{B108} &> -1 \text{ K and} \\ R_{006}/R_{016} &< 0.8 \text{ and} \\ T_{B087} - T_{B108} &> -1 \text{ K,} \end{aligned} \quad (5)$$

and

$$\begin{aligned} T_{B120} - T_{B108} &> -1 \text{ K and} \\ R_{006}/R_{016} &< 0.7 \text{ and} \\ T_{B087} - T_{B108} &> \min(-1, 2.5 - 18R_{006}) \text{ K.} \end{aligned} \quad (6)$$

The ratio of the fractional reflectances in the 0.6 and the 1.6 μm channels ( $R_{006}$  and  $R_{016}$ ) is used to discriminate dust from other aerosols such as smoke, which tend to be smaller and hence to scatter more at shorter wavelengths (Evan et al., 2006): for smaller smoke particles this ratio will be larger. It can also be used to help to filter clouds from dust (Heidinger et al., 2004). Over most bright desert surfaces the ratio is generally less than 0.7, but over some darker surfaces the ratio may be greater, potentially making it more difficult to detect weak to moderate dust loadings over such regions. At higher dust loadings the dust signal will dominate.

#### 2.4. Quantification of the SEVIRI DAOD

Retrievals of DAOD over land from SEVIRI are made using observations in the 10.8 and 13.4 μm channels. The method is described in detail in BR09 and is optimised for arid and semi-arid regions. It requires both a dust detection and a cloud detection scheme to be implemented before application. Here, cloud is flagged if it is detected using either the scheme developed by Derrien and Le Gléau (2005), which uses both infrared and visible information, or by the standard GERB detection scheme (Ipe et al., 2004) which uses visible information only. Briefly recapping the DAOD retrieval method, the first step requires the generation of pristine-sky  $T_{B108}$  values, denoted  $T_{B108\text{dfe}}$ , for each pixel and time-slot where a retrieval is performed. Retrievals are performed when cloud is not detected or dust is detected (at high dust loadings the cloud flags can be activated – Section 3), when the solar ( $\theta_s$ ) and viewing ( $\theta_v$ ) zenith angles are less than 70°, and when the GERB surface type mask indicates that the pixel is land. To generate  $T_{B108\text{dfe}}$ , for each time slot and pixel, the most pristine  $T_{B108}$  observation over a prior 28 day rolling window is identified. This time period has been chosen to maximise the chance of identifying a suitable pristine-sky day while not being so long that the surface conditions – for example vegetation cover – vary significantly over this time. In transition periods, particularly in the Sahelian region, this latter condition may not be fully met. The effects of changes in skin temperature and total column water vapour between this observation and the time at which the retrieval is actually being performed are then accounted for. Here we use 6-hourly skin temperature and total column water vapour fields from ERA Interim reanalyses, interpolated to the given times and

pixel locations to provide the atmospheric variability information. The dust only impact on the observed  $T_{B108}$  value,  $\Delta T_{B108}$  is then obtained using:

$$\Delta T_{B108} = T_{B108\text{dfe}} - T_{B108}. \quad (7)$$

A similar quantity is also derived for the 13.4 μm channel, and the ratio of  $\Delta T_{B108}/\Delta T_{B134}$  is used to derive the DAOD at 550 nm. The addition of the 13.4 μm information takes some account of the effect of variations in dust height on the brightness temperature signals. For a given day-time observation, as dust loading increases an associated decrease in surface temperature relative to pristine conditions would be expected. Hence one might anticipate a bias towards artificially high DAODs at higher dust loadings since  $T_{B108}$  will be reduced both by the reduced surface emission and the presence of the dust itself. However, any impact of a dust induced reduction in surface temperature on the  $\Delta T_{B108}$  values should be mitigated by two factors. First, observed surface temperatures are assimilated into the ERA-Interim fields such that  $T_{B108\text{dfe}}$  will also implicitly include at least part of any dust induced surface temperature change. Second, under heavy dust loadings, when any surface cooling effect would be expected to be largest, the majority of the observed signal comes from the dust itself and is thus relatively insensitive to the surface temperature.

### 3. Dust observations

#### 3.1. Dust detection observations

Maps of dust and cloud detections for January and June 2009 are presented in Figs. 1 and 2. Detections are not carried out over water, so seas and lakes appear white, although some rivers such as the Nile are narrow enough (sub-pixel) that they are misidentified as land. Across the domain the number of cloud detections is greater in June than in January, especially over the Sahel and the southern Sahara. This is due to the West African Monsoon (Redelsperger et al., 2006), which is at its height in June and July. January is one of the months of the West African dry season.

Dust should primarily be found in the central Sahara and in the Sahel nearest the major source regions (e.g. (Prospero et al., 2002)), but especially in January this is not necessarily the case in the dust detection flags (Fig. 1a, c, and e). The dust flagging suggests that the most frequent regions of dust occur in very specific locations, particularly in various parts of the northern Algerian Sahara, along the Libyan and Egyptian coasts, in Iraq, in Yemen, and in an arc in central Saudi Arabia. These are static and highly structured features, which do not move during the diurnal cycle, contrary to what would be expected of atmospheric dust. For sporadic atmospheric dust events, we would expect a more amorphous region of dust, occurring on a smaller fraction of the days during the month. They are also unlikely to be dust from wadi systems, since low dust is not readily retrieved due to the weak temperature contrast. Furthermore, many of the static features occur in mountainous and/or rocky areas (some of which follow lines of hills, as in Arabia) which would not be expected to be significant or regular sources of dust. Most of these areas have not been identified as specific sources of dust or as regions of high dust loading. For example, using satellite data from the Total Ozone Mapping Spectrometer Prospero et al. (2002) identify Libya's eastern desert, spilling over into western Egypt, as an area of high dust loading. Note that TOMS observations have their own shortcomings, such as their insensitivity to aerosol in the lowest layer of the atmosphere (Torres et al., 2002), and hence may be insensitive to low-altitude dust in the winter (Liu et al., 2008). Maps of monthly mean TOMS aerosol index values, as presented in Fig. 2 by Engelstaedter and Washington (2007), show very little dust activity in the north of the Sahara during the winter: the static features seen in the SEVIRI flags

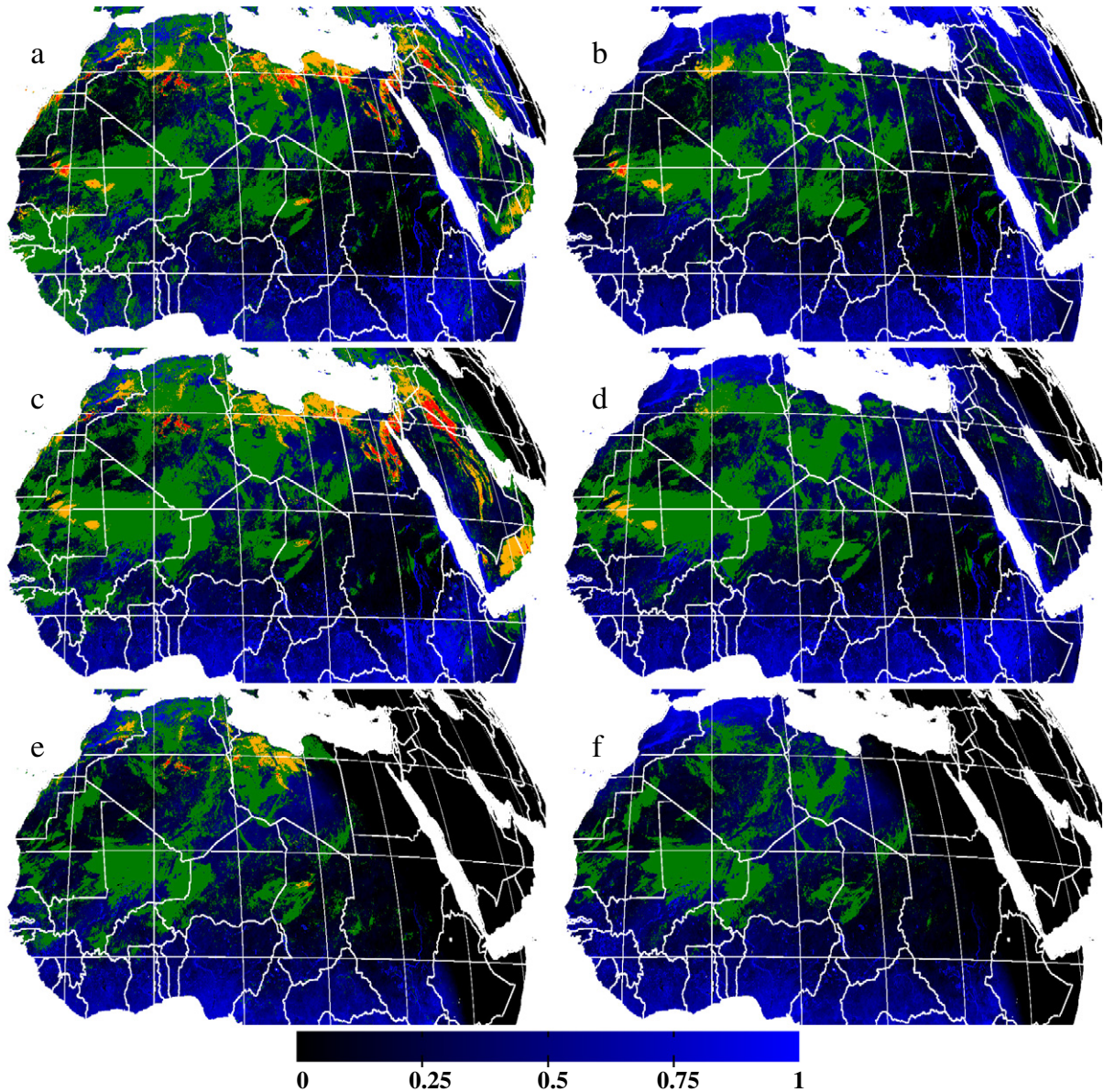


**Fig. 1.** Maps of dust and cloud flagging over land, for 'v1' dust detection (left) and for 'v2' (right), for January 2009. (a), (b) 1000 UT; (c), (d) 1200 UT; (e), (f) 1400 UT. The green, orange, and red colours indicate the number of occurrences of dust flags during the month at this time: green indicates dust on 1–10 days during the month, orange indicates dust on 11–20 days, and red indicates dust on >20 days. The intensity of the blue channel indicates the fractional occurrence of cloud detections (for pixels flagged as dust, the cloud detection is not shown). Black indicates no detections of either dust or cloud at any time during the month over land. The terminator line in the top right corner delineates the 70° solar zenith angle contour line. The latitude and longitude lines are spaced by 10°, running from 10 to 30°N over northern Libya and from 10°W to 60°E off the eastern tip of Arabia.

are not present in the TOMS observations, nor do they have the sharp structure observable in the SEVIRI dust detection imagery. Visual identification of sources from SEVIRI also supports this basic pattern (Schepanski et al., 2007). Similarly in Arabia, the main areas of dust loading are in Saudi Arabia's eastern desert next to the Persian Gulf and the Rub al Khali next to the UAE/Omani border (Washington et al., 2003), rather than in the well defined central crescent following the Jabal Tuwayq escarpment displayed in Fig. 1a and c.

These potentially anomalous features are predominantly triggered by the dust flag specified by Eq. (6), specifically by the relationship between  $T_{B087}$ ,  $T_{B108}$ , and  $R_{006}$ . These areas can be discriminated from the surroundings by the high values of  $T_{B087}$ , a consequence of high emissivities in the 8.7  $\mu\text{m}$  channel. Hence we hypothesise that these stationary features indicate surface contamination of the dust detection algorithm (henceforth these rocky surface contamination features will be denoted RSCFs).

In June the RSCFs tend to occur most often towards the end of the day, as seen in Fig. 2: around local noon in Egypt and Libya (1000 and 1200 UT) there are few detections, but the detections flare briefly towards the end of the day at 1400 UT. A similar pattern is also observed in Yemen. This pattern is triggered by the  $T_{B120} - T_{B108}$  difference in Eq. (6), which responds to both surface temperature and column moisture. This difference will tend to be larger in colder, drier conditions, although in the generally arid locations sampled here the surface temperature effect will dominate. In June, the generally warmer surface temperatures, coupled with their marked diurnal cycle means that the dust flag is typically deactivated during the middle of the day. Conversely, in January, surface temperatures are lower such that the criteria are generally fulfilled at all times of day.

The presence of the RSCFs is a consequence of the assumption of large-scale surface homogeneity over a sandy desert surface made by the dust detection algorithm. The  $T_{B120}$ ,  $R_{006}$ , and  $R_{016}$  channels

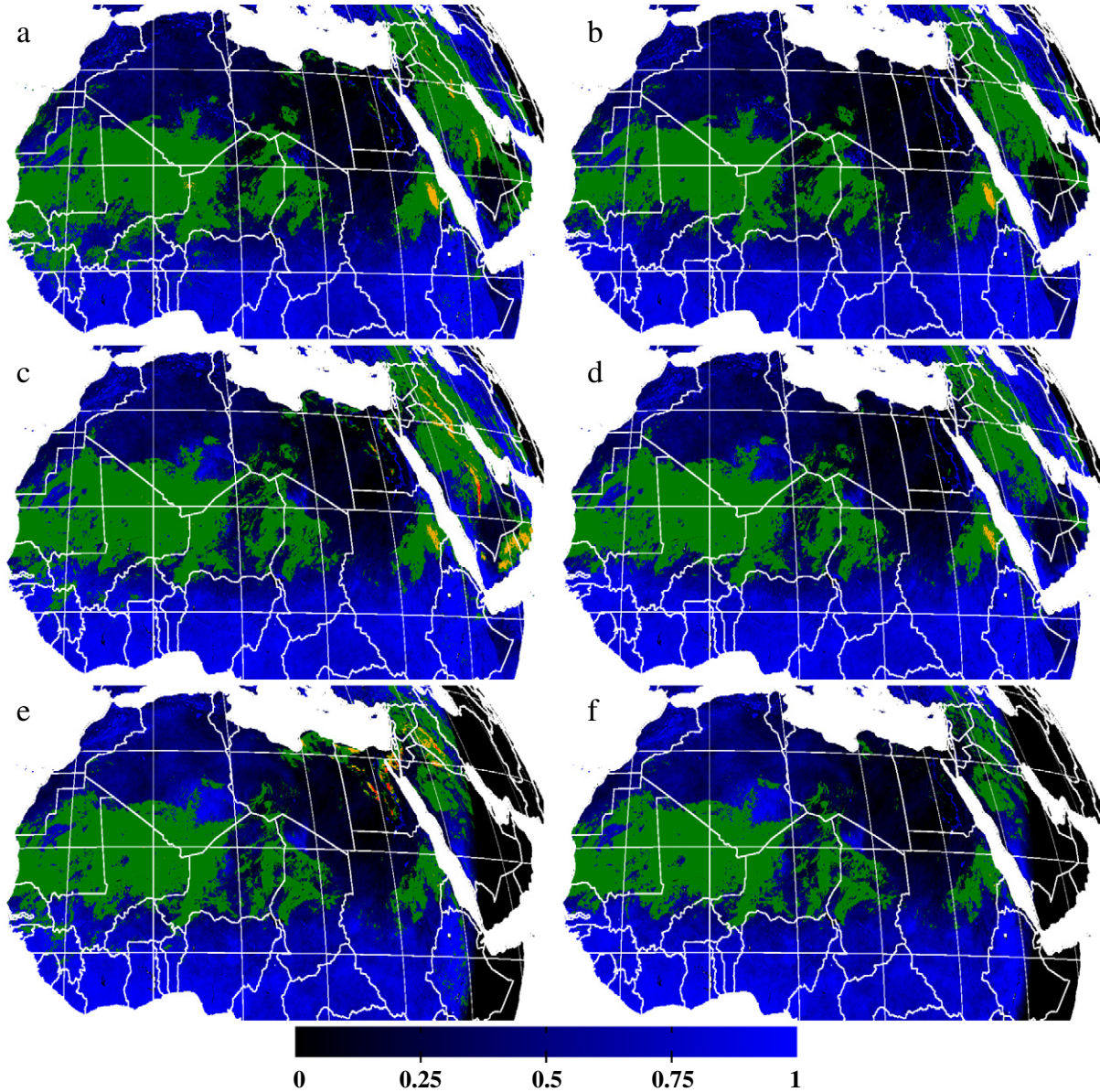


**Fig. 2.** As for Fig. 1, for June 2009.

are used to filter cloud, while the  $T_{B039}$  channel is used to detect dust under specific conditions. The  $T_{B087}$  channel attempts to account for the surface properties, but only by contrasting the size of the dust/sand grains in the atmosphere and on the surface: this does not account for other surface types, such as rock and vegetation. What is required is a method to account for other types of surface feature, so that dust is not falsely flagged. In order to screen out the RSCFs, the following condition (Ashpole & Washington, 2012) is added to the criteria given by Eqs. (5) and (6), both of which are already sensitive to  $T_{B108}$ :

$$(T_{B108} - T_{B087}) - \overline{(T_{B108} - T_{B087})} < -2 \text{ K}, \quad (8)$$

where the monthly average cloud-screened value of  $\overline{(T_{B108} - T_{B087})}$  is calculated independently for each time-slot during the diurnal cycle. We refer to this new dust detection scheme as the version 2 ('v2') scheme, as opposed to the standard version 1 ('v1') scheme. Resultant values of DAOD are also discriminated by their use of the v1 or v2 dust detection, although the change should not significantly affect the DAODs, since the DAODs are calculated where there is dust flagged

or where there is no cloud. This method aims to mitigate the effect of areas of high  $8.7 \mu\text{m}$  emissivity by constraining dust detections to times when the deviation from the monthly average of the brightness temperature difference exceeds a defined threshold. When the difference is less than this threshold, then the brightness temperatures are sufficiently close to the climatological values that they are regarded as surface features.

The right-hand panels in Figs. 1 and 2 map the monthly dust detections using the v2 flags, for January and June 2009. The surface filtering can be seen to have a more significant effect in January, filtering features in Morocco, Algeria, Libya, Egypt, and across the Arabian peninsula. Also screened out is the surface of the Bodélé Depression ( $\sim 17^\circ\text{N}$ ,  $17^\circ\text{E}$ ) in Chad which is shaped as a ring, but not the ejected dust which travels south-westwards from the Depression. This moves during the diurnal cycle, even at a monthly timescale, indicating the typical daily timings of dust uplift and transport from the Bodélé. In June some of the major dust features are a large and hazy area of the central Western Sahara, and regular dust storms in eastern Sudan (Prospero et al., 2002). The geographical distribution of the v2 dust detections matches well with maps of dust uplift (Marsham et al., 2011), indicating the

role of low-level jets, monsoon surges and cold pools in the formation of dust events.

Some other surface features may still be flagged by the v2 detection scheme. Such features are the Grand Ergs Occidental ( $\sim 26^\circ\text{N}$ ,  $0^\circ\text{E}$ ) and Oriental ( $\sim 27^\circ\text{N}$ ,  $8^\circ\text{E}$ ) of northern Algeria, the Idhan Murzuq sand sea of south-western Libya ( $\sim 25^\circ\text{N}$ ,  $13^\circ\text{E}$ ), and a large area of central and south-eastern Mauritania. These areas are flagged less often than the rockier areas, but are also potentially spurious, due to their static nature. The equation that triggers the dust flag is specified by Eq. (4), relating to  $T_{\text{B}039}$ . At high solar zenith angles the surface albedo is increased (Wang et al., 2005), which amplifies the solar reflectance contribution to the  $T_{\text{B}039}$  channel. Since these areas have some of the highest land climatological reflectances (see top panels of Fig. 3), these areas are also the most sensitive to this effect. Since this is a comparatively rare effect, affecting smaller areas and shorter timescales than the  $8.7\ \mu\text{m}$  RSCFs, and since the sandy texture of these surfaces makes it particularly difficult to discriminate here between surface sand and lofted dust, it is not proposed that these features be screened out.

### 3.2. Surface characteristics and their impacts on dust detection

To further explain why these RSCFs occur where they do, it is instructive to look at maps of monthly surface reflectance (Fig. 3a and b) and surface emissivity (Fig. 3c–h). The latter are provided by the University of Wisconsin, and derived from MODIS data (Seemann et al., 2008). Monthly mean emissivities are provided for ten wavelengths at a spatial resolution of  $0.05^\circ$ . To find the emissivity at  $3.9$ ,  $8.7$  and  $12.0\ \mu\text{m}$  linear interpolation can be carried out between the provided channels ('hinge' points). As noted by Seemann et al. (2008), while this will not give sufficient resolution for the values to be appropriate for use with hyper-spectral instruments such as AIRS or IASI, the overall spectral shape is captured well and should thus be adequate to give a good indication of the surface emissivity over the (wider) SEVIRI wavelength bands. These are also bilinearly interpolated to the SEVIRI grid for direct pixel-to-pixel comparison. The climatological surface reflectances are provided by RMIB at a wavelength of  $600\ \text{nm}$  (Derrien & Le Gléau, 2005). As a whole, arid regions tend to have higher reflectances

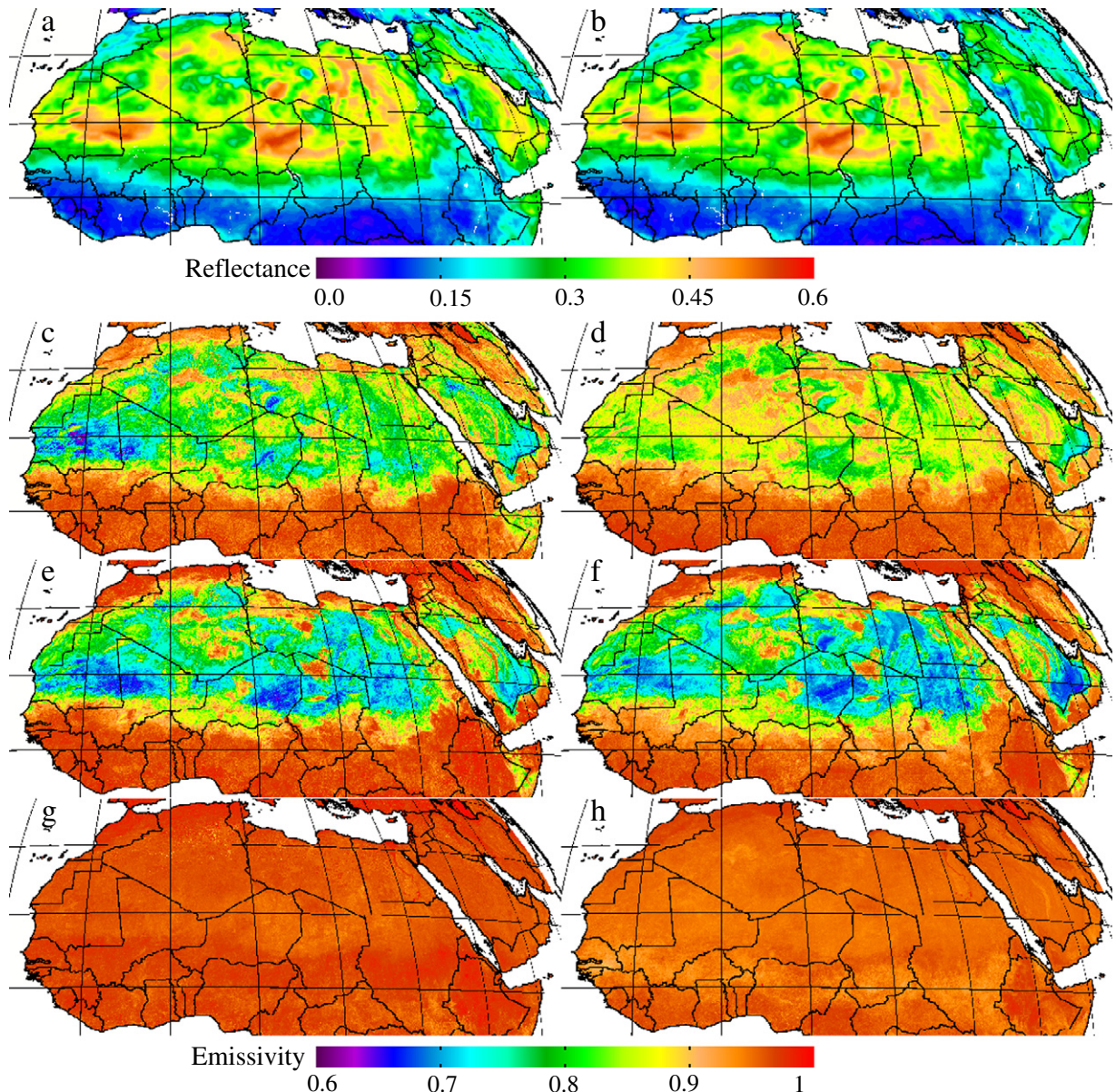


**Fig. 3.** Maps for January 2009 (left) and June 2009 (right) of surface reflectance and emissivity, using climatological reflectance data provided by RMIB, and emissivity data derived from MODIS (Seemann et al., 2008). (a) and (b) surface climatological reflectance at  $600\ \text{nm}$ ; (c) and (d) surface emissivity at  $3.9\ \mu\text{m}$ ; (e) and (f) surface emissivity at  $8.7\ \mu\text{m}$ ; (g), (h) surface emissivity at  $10.8\ \mu\text{m}$ . The emissivity at  $12.0\ \mu\text{m}$  is generally greater than  $10.8\ \mu\text{m}$ , and is more geographically homogeneous.

and lower emissivities than other surface types. Emissivities at the longer wavelengths (10.8 and 12.0  $\mu\text{m}$ ) vary little spatially, whereas the shorter wavelengths (3.9 and 8.7  $\mu\text{m}$ ) show much more spatial structure over the desert regions, which have some of the lowest land surface emissivities on the planet (Jin & Liang, 2006). Mountains tend to have higher emissivities and lower reflectances than the surrounding desert, while sand seas tend to have the lowest emissivities and the highest reflectances. More complicated are the rocky deserts, or hamadas, which can have high emissivities but still reasonably high reflectances: these are the areas where the v1 algorithm tends to spuriously detect dust.

The RSCFs are predominantly a product of the high emissivities in the 8.7  $\mu\text{m}$  channel, coupled with moderately high reflectances, which are sensitive to the increase in albedo caused at high  $\theta_s$  (Wang et al., 2005) for bare soil surfaces. Density histograms of dust detections in relation to surface emissivity and climatological reflectance are presented in Fig. 4. Fig. 4a and b indicate the frequency of varying dust loadings, specified by the normalised dust detection per pixel during the month, against the 8.7  $\mu\text{m}$  emissivity. Peaks are observed in the v1 detections at emissivities of 0.7 and 0.96, with the latter being responsible for the pixels which have the most frequent detections. There is a slight positive correlation of  $\sim 0.2$  between the emissivity and the v1 dust flagging. An initial assumption might be that there should be no correlation between atmospheric dust and surface features if the land and atmosphere were well decoupled. However, the major source regions for dust are dried lake beds and to a lesser extent sand seas, which have lower emissivities, so a priori we would expect a negative correlation. This is the case for the v2 flags, where many of the detections for pixels with emissivities  $> 0.8$  are suppressed in relation to v1. Similarly, for the climatological reflectance (Fig. 4c and d), the sand seas have the highest reflectance, so we would expect a positive correlation: the v2 detections have a much stronger positive correlation with climatological reflectance than do the v1 detections.

### 3.3. Sensitivity of DAODs to dust detection

While it appears that changing from v1 to v2 will strongly impact the frequency of dust detections, from the point of view of assessing dust radiative impact, a useful question to ask is how strongly this impacts the dust loading within the atmosphere. Recall that the BR09 dust algorithm used the v1 dust detection scheme to identify strong

dust events that were erroneously flagged as cloud. DAOD retrievals were also performed on locations where neither dust nor cloud were identified, to try to avoid missing smaller dust events which would not be expected to be captured by the detection scheme.

The value of applying the v2 dust detection method for DAOD, as opposed to the v1 detection, or alternatively having no dust detections at all, can be illustrated using a suitable case study. One such event, chosen for its mix of strong dust events, cloud, and surface features, occurred on the 17th January 2010, when three extensive dust storms spread across Niger and eastern Mali (Fig. 5a). Dust is detected by the v1 detection in areas where the RGB imagery gives no indication of the presence of dust, which we might expect to appear pink. Note the obvious surface features such as the arc in Saudi Arabia and a region of north-western Egypt in the ‘pink-dust’ image which are flagged as dust in the v1 detection, but not in the v2: this provides a qualitative justification for regarding these regions as spurious.

Maps of the corresponding DAOD are presented in Fig. 6. As sensitivity studies, also presented are a ‘no-dust’ scenario, in which the pristine-sky window is built up without any input from the dust detection, and an ‘only-dust’ scenario, in which the only pixels on which  $\Delta T_{B108}$  and DAOD are calculated are those pixels where dust is flagged. The need for a dust detection is readily apparent from the no-dust scenario, since the areas of heaviest dust loading (with a high DAOD of  $\sim 3$ ) are flagged as cloud.

Could this really be cloud? These areas are marked as deep pink by the pink-dust imagery, while the total column water vapour from ERA-Interim is very low (Fig. 5d), dropping to values of  $\sim 5 \text{ kg m}^{-2}$  over eastern Mali. This gives confidence in the validity of the dust detection.

In this case study, the differences between the v1 and the v2 DAODs are negligible, since the areas where the RSCFs affect the detection tend to be cloud-free. It is in the only-dust cases where the largest differences can be seen between the two dust detection schemes. While there is good agreement for the large-scale dust events, the v1 detection gives rise to numerous scattered ‘dust’ pixels in the Atlas mountains, in northern Libya and Egypt, and over the arc in Arabia. These were all areas highlighted as RSCFs. Although the pink-dust image is itself not infallible, it also suggests that these pixels are not dusty.

Should we perform retrievals only over the flagged points? Comparison with the pink-dust image suggests not, since large areas of

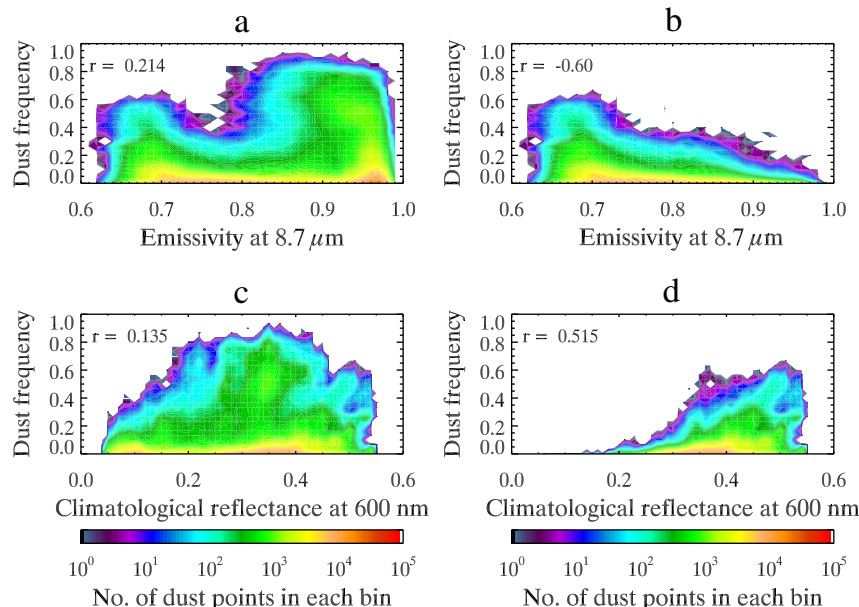


**Fig. 4.** Density histograms of pixel dust flag dependencies on emissivity and reflectance, for January 2009 at 1200 UT. Left is v1, right is v2. (a and b) Emissivity at 8.7  $\mu\text{m}$  against the normalised monthly frequency of dust flags. (c and d) Climatological reflectance against the normalised monthly frequency of dust flags.

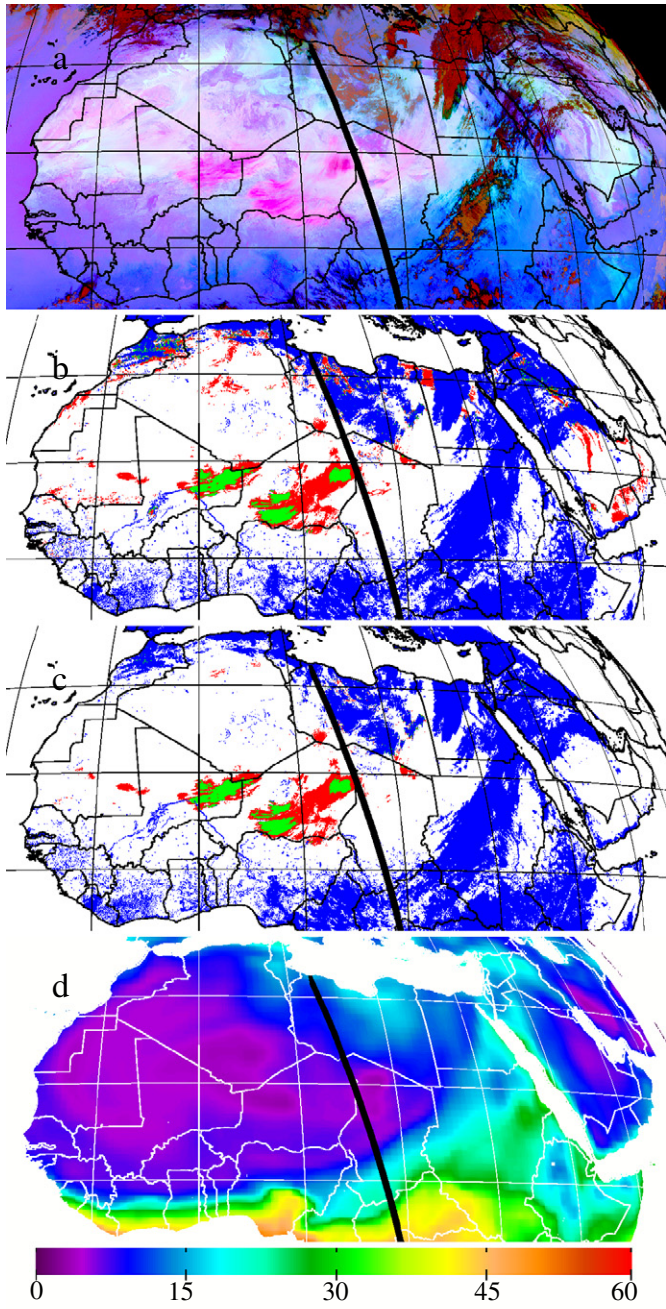


**Fig. 5.** Dust activity at 1200 UT on 17th January 2010: (a) the pink-dust RGB image; (b) v1 dust and cloud detections; (c) v2 dust and cloud detection; (d) the total column water vapour over land ( $\text{kg m}^{-2}$ ), as given by ECMWF ERA-Interim (Dee et al., 2011). For the detections red is dust, blue is cloud, green is overlapping dust and cloud, and white indicates no detection. The solid black line represents the CALIPSO track, at  $\sim 1230$  UT.

the West African Sahara (northern Mauritania and Mali) appear to have a pink haze of dust, which is thin enough not to trigger the dust detection algorithm. Hence the only-dust DAOD retrieval ignores these areas, despite the presence of dust with a DAOD of  $\sim 1$  as shown in Figs. 6a and b.

Lidar observations from the Cloud-Aerosol Lidar and Infrared Pathfinder Satellite Observations instrument, CALIPSO (Winker et al., 2009), may be used to retrieve aerosol height (Liu et al., 2008) and AOD. The Saharan CALIPSO observations for the 17th January 2010 are presented in Fig. 7. Very little dust is retrieved over Libya, where the v1 detections flag dust, supporting the argument that

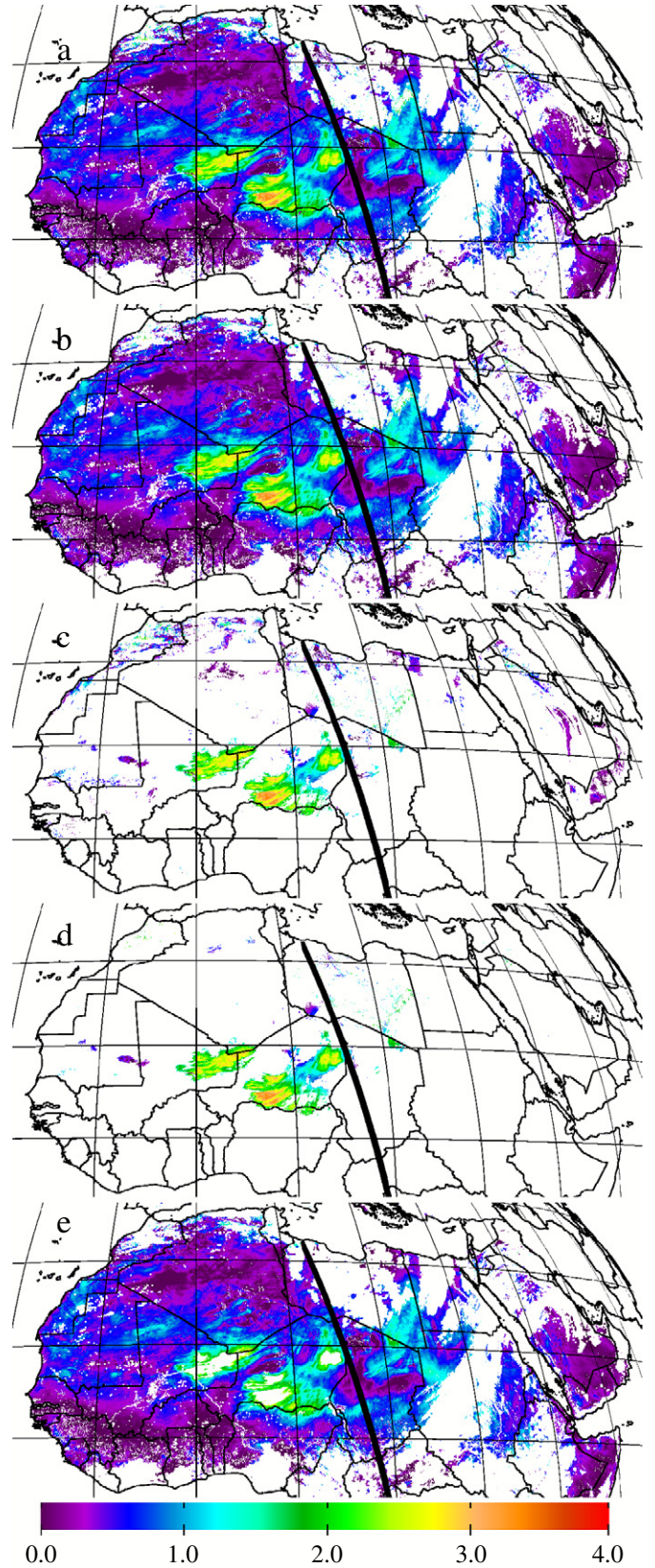


**Fig. 6.** DAOD at 1200 UT on 17th January 2010: (a) v1 DAOD; (b) v2 DAOD; (c) the v1 'only-dust' case; (d) the v2 'only-dust' case; (e) the 'no-dust' DAOD case. Included is the CALIPSO track at  $\sim 1230$  UT.

these detections are spurious. Meanwhile a dust layer is detected from  $\sim 10$  to  $24^\circ\text{N}$ , which also agrees with the SEVIRI dust detections and the high DAODs in this region, although at  $\sim 18^\circ\text{N}$  some cloud is

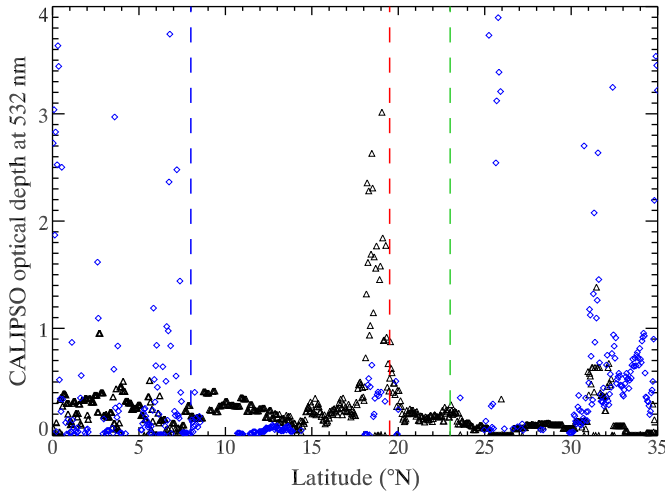


**Fig. 7.** CALIPSO optical depth at 532 nm at an equator crossing time of ~1225 UT on 17th January 2010. Saharan AOD measurements start at a latitude of ~10°N, and end at ~30°N. Black triangles denote aerosol optical depth, blue diamonds denote cloud optical depth. The dashed lines denote (from south to north) the borders of the Central African Republic and Chad, Chad and Niger, and of Niger and Libya. To emphasise the AOD, the optical depth maximum has been limited to 4; only 7 cloud optical depths exceed 4 (peaking at an optical depth of 8.5).

also detected amongst the heavier aerosol loading. These dust plumes extend from the surface to a maximum altitude of ~2 km.

#### 3.4. DAOD thresholds of the dust flags

The ‘only-dust’ DAOD results above indicate that there is a minimum threshold of dust loading required before the dust detection flags are triggered, while the ‘no-dust’ results indicate that there is a maximum threshold of dust loading before the cloud detection flags are (falsely) triggered. Fig. 8 shows the probability density functions (PDFs) of DAOD with respect to the coincident dust flags and coincident non-dust (i.e. dust and cloud-free) pixels, for selected regions within North Africa and Arabia during January 2009. There are 100 bins in the DAOD histogram, with a bin width of 0.1, and the highest retrieved DAOD during the month is 5.55. One would expect a reduction in the number of non-dust pixels as DAOD increases (dashed lines). Conversely, above a certain threshold, below which the detection scheme is insensitive, one would expect the number of dusty pixels to increase as DAOD increases, but an overall reduction in the PDF at high DAOD due to the scarcity of large dust events. Cloud flags should follow a similar pattern to the dust flags. Hence where the dashed and the solid lines cross each other can be considered a threshold value for the dust or cloud loading at which a pixel is more likely to be flagged as dusty or cloudy than pristine.

To ensure consistency in the derived dust record, we would like the value of this threshold to be approximately constant for all the regions covered. The threshold should not vary by region since this would indicate that the atmospheric dust detection is dependent on the regional surface. Across the domain the threshold value of DAOD is 1.9 in the v1 dust scheme, 2.0 in the v2 scheme: this reinforces our earlier point that the dust detection scheme performs best at high dust loadings, whereas it is liable to miss weaker dust events. These values of the threshold are relatively consistent for some of the sandier deserts (the ‘Sahara’ regions) where surface contamination is less significant, but are more divergent over the region covering northern Libya and northern Egypt, and the region covering Arabia, both of which contain higher fractional coverages of RSCFs. Over the northern Libyan region, the threshold values are 1.2 in the v1 scheme, and 1.8 in the v2 scheme. As seen earlier, the RSCFs tend to result in false detections which reduce the DAOD threshold. The v2 scheme overrules

this spurious flagging, making the region more consistent with the rest of the desert and the domain: on this basis, the v2 scheme is preferable to the v1, since it triggers dust detection at consistent dust loadings, independent of the surface type.

The coincident cloud flags and DAOD comparison is provided by the red and gold lines in Fig. 8. Above a specific ‘cloud threshold’ of DAOD, all of the dust points are also flagged as cloud: across the domain the cloud thresholds of DAOD are 3.4 for both the v1 and the v2 schemes. Above this value of DAOD, unless the dust detection scheme is included, the retrieval algorithm would assume that the thick dust is in fact cloud and hence no DAOD retrievals would be performed. Without the dust detection scheme this would be a significant handicap, since thick dust, which has the largest instantaneous effect on the radiation budget, would not be accounted for.

A small number of pixels at the higher end of the DAOD range are not flagged as dust (especially in Fig. 8c and f): these are located over water features, such as the river Niger in Mali (especially Lac Fagurbine west of Tombouctou, ~17°N, 4°W) and Lake Nasser in Egypt. Variability in water levels may affect the pristine-sky value  $T_{B108\text{dfe}}$ : if the pixel is dry/bare at some point during the pristine-sky window, then there will be a strong contrast in  $T_{B108}$  between this value and the values observable when the pixel is inundated.

#### 3.5. Monthly DAODs over North Africa

Similar to the results seen in Section 3, on a monthly timescale, the effects on the resultant DAOD from the differences between the v1 and the v2 dust detection schemes are small (Fig. 9), even when the numbers of dust detections differ significantly. A plot of the differences indicates that the most substantial deviations of the v2 from the v1 DAODs are, as expected, in northern Libya, Egypt's Sinai peninsula, and in Iraq and Arabia.

Dust loadings are low in January across most of the Sahara; despite several dust outflows from the Bodélé Depression in Chad, on the monthly average in 2009 this area is relatively quiet. There is a more frequent area of moderate dust loading further west, on the border between Mauritania and Western Sahara, a result of frequent cloud-free days and occasional dust events in January 2009. This is a feature which is not so apparent in 2008 or 2010, and which has not been identified as a major source area (e.g. (Prospero et al., 2002; Schepanski et al., 2009)). Meanwhile in June (Fig. 10), there is a large area of dust loading over the western half of the Sahara, stretching from western Niger across southern Algeria and northern Mali into eastern Mauritania, most active in the morning. The morning peak in dust loading is consistent with modelled peaks in the low-level jet (a key trigger mechanism for dust uplift) between 0700 and 1000 UT (Marsham et al., 2011), which disperses as the day progresses. A more spatially limited area of high DAOD is observable in eastern Sudan at 1000 UT, local noon. These two regions correspond well with the areas of frequent dust detection as shown in Fig. 2.

## 4. AERONET validation of the SEVIRI products

Building on BR09, in order to assess the quality of the SEVIRI DAOD, we compare the observations against the AERONET network of sun-photometers (Holben et al., 1998), which measure AOD at a number of wavelengths. The AERONET sites available within the desert and near-desert regions of North Africa and the Middle East since 2008 are listed in Table 3, and mapped in Fig. 11. Level 2 data are used where available, otherwise level 1.5 data are used. For comparison with SEVIRI, each site is considered to have a ‘radius of influence’ of 25 km over which the SEVIRI data are averaged, while the AERONET data are averaged over the number of data points within 15 minutes of the SEVIRI timeslot. Sites on islands and on coasts have been neglected, where the variability in the sub-pixel surface type can distort the detection. Other sites have been left out because the aerosol type is dominated

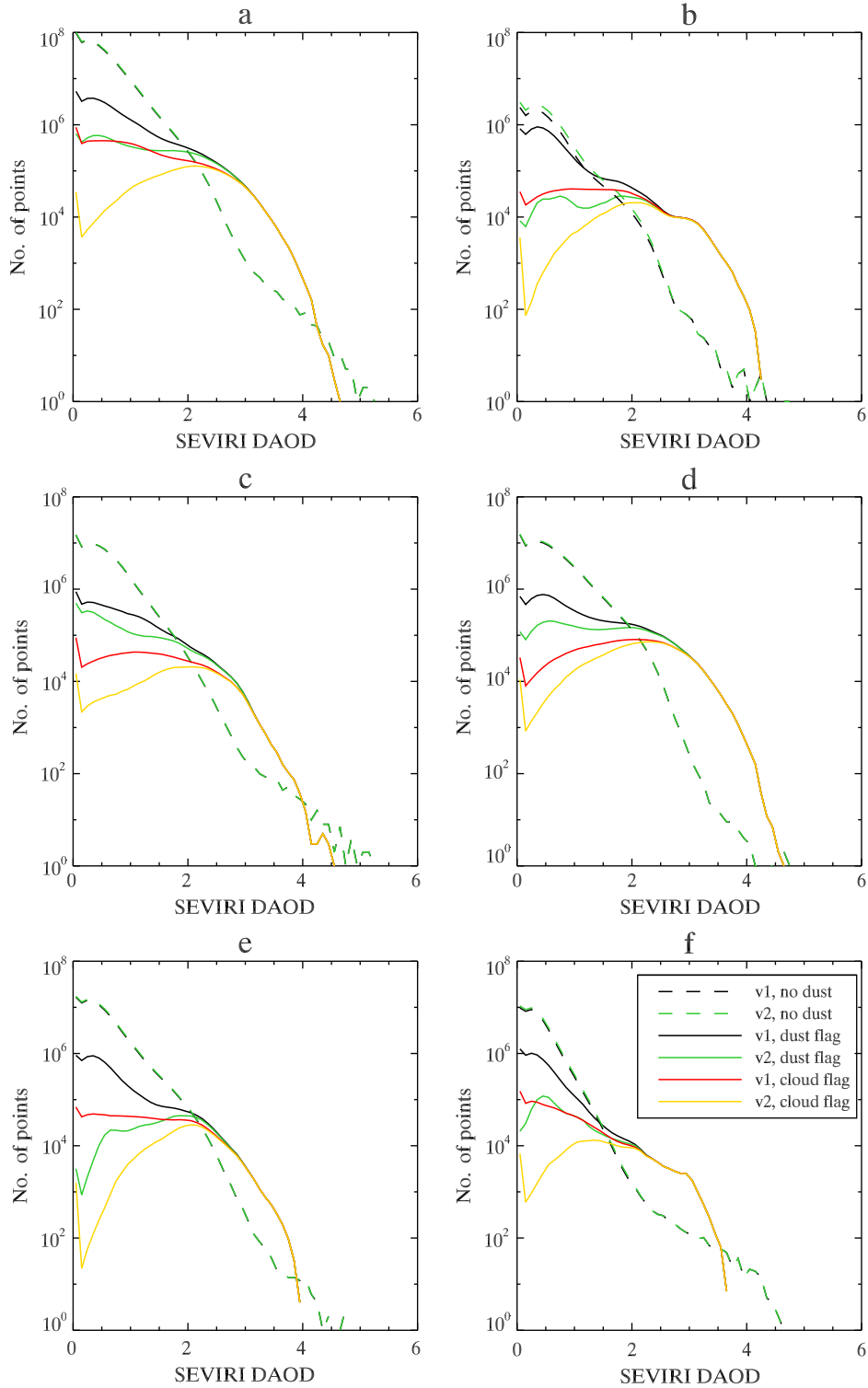


**Fig. 8.** Frequency of pixel matches between dust flags and DAOD detections, for January 2009. The dashed lines indicate the frequency of pixels with retrievals where dust is not flagged, while the solid black and green lines indicate where dust is flagged. The solid red and yellow lines indicate where both dust and cloud are flagged, which are subsets of the respective solid black and green lines. (a) Full domain; (b) 'northern Libya' ( $27\text{--}33^\circ\text{N}$ ,  $9\text{--}30^\circ\text{E}$ ); (c) 'western Sahara' ( $13\text{--}35^\circ\text{N}$ ,  $18^\circ\text{W}\text{--}0^\circ\text{E}$ ); (d) 'central Sahara' ( $13\text{--}35^\circ\text{N}$ ,  $0\text{--}18^\circ\text{E}$ ); (e) 'eastern Sahara' ( $13\text{--}35^\circ\text{N}$ ,  $18\text{--}36^\circ\text{E}$ ); (f) 'Arabia' ( $13\text{--}35^\circ\text{N}$ ,  $36\text{--}60^\circ\text{E}$ ).

by aerosols other than dust such as urban pollutants (e.g. Cairo EMA) or biomass burning (e.g. Ilorin in Nigeria). Following Dubovik et al. (2002) we filter the AERONET data such that only data points when the Ångström coefficient (between 440 and 870 nm)  $\alpha \leq 0.6$  and  $\tau_{size1020\text{ nm}} \geq 0.2$  are included, so as to specify data influenced primarily by mineral dust. This may mean that small dust events in the AERONET record are

missed but it mitigates against including non-dusty aerosol events such as biomass burning (often seen over the southern part of this region in boreal winter) and also aerosol from local pollution sources. There is no lower threshold for the SEVIRI DAODs, since the SEVIRI retrieval scheme is nominally designed only to be sensitive to mineral dust (BR09), unlike the more general aerosol retrieval carried out by

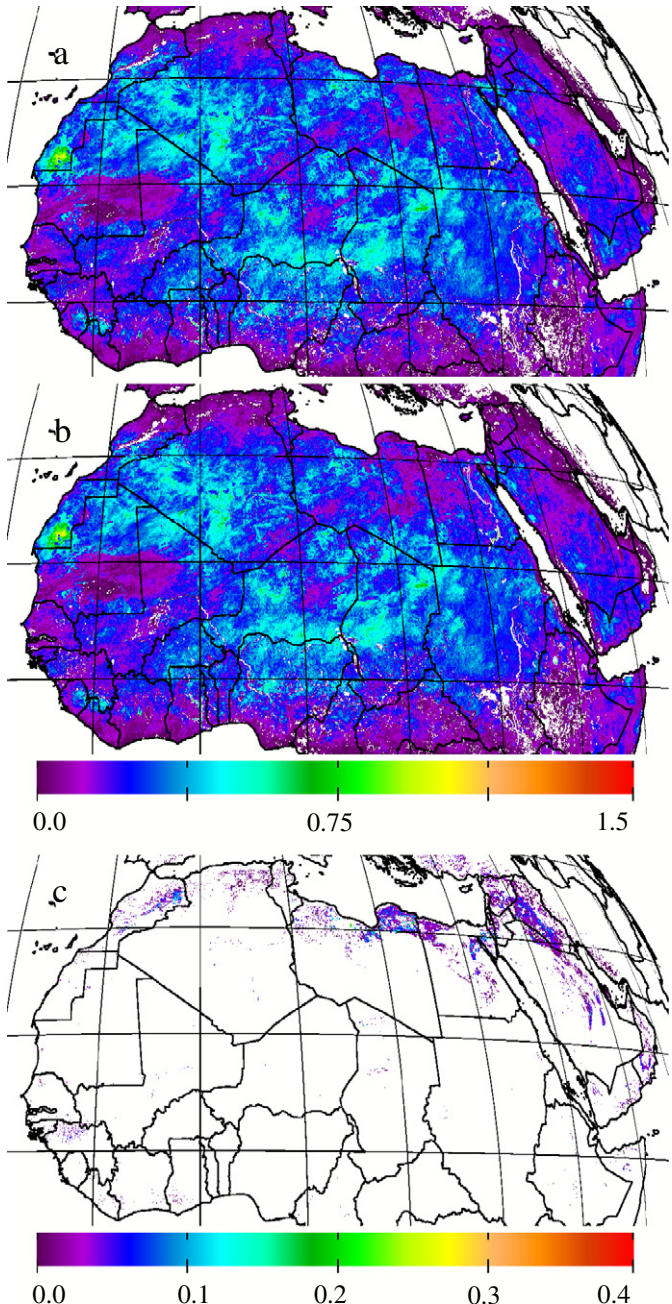


**Fig. 9.** Maps of monthly average dust DAOD at 550 nm, for (a) v1 dust detection, (b) v2, (c) the difference between the two versions ( $v1 - v2$ ), for January 2009, at 1200 UT.

AERONET. AERONET optical depths are not measured at 550 nm, whereas they frequently are at 675 nm; therefore we obtain AOD at 550 nm,  $\tau_{550}$ , using:

$$\tau_{550} = \tau_{675} (675/550)^\alpha, \quad (9)$$

where  $\alpha$  is the Ångström coefficient (Eck et al., 1999). In practice the Ångström coefficient between 440 and 870 nm is used, as provided by the AERONET data (BR09). Note also that the AERONET data is significantly limited in its spatial distribution, with very few sites in the central Sahara, and only five sites in the Sahel, the region with the most coverage. Moreover, few of the sites are near any of the RSCFs, so the capability of AERONET to evaluate the effects of the v2 dust detection as contrasted with the v1 detection is limited.

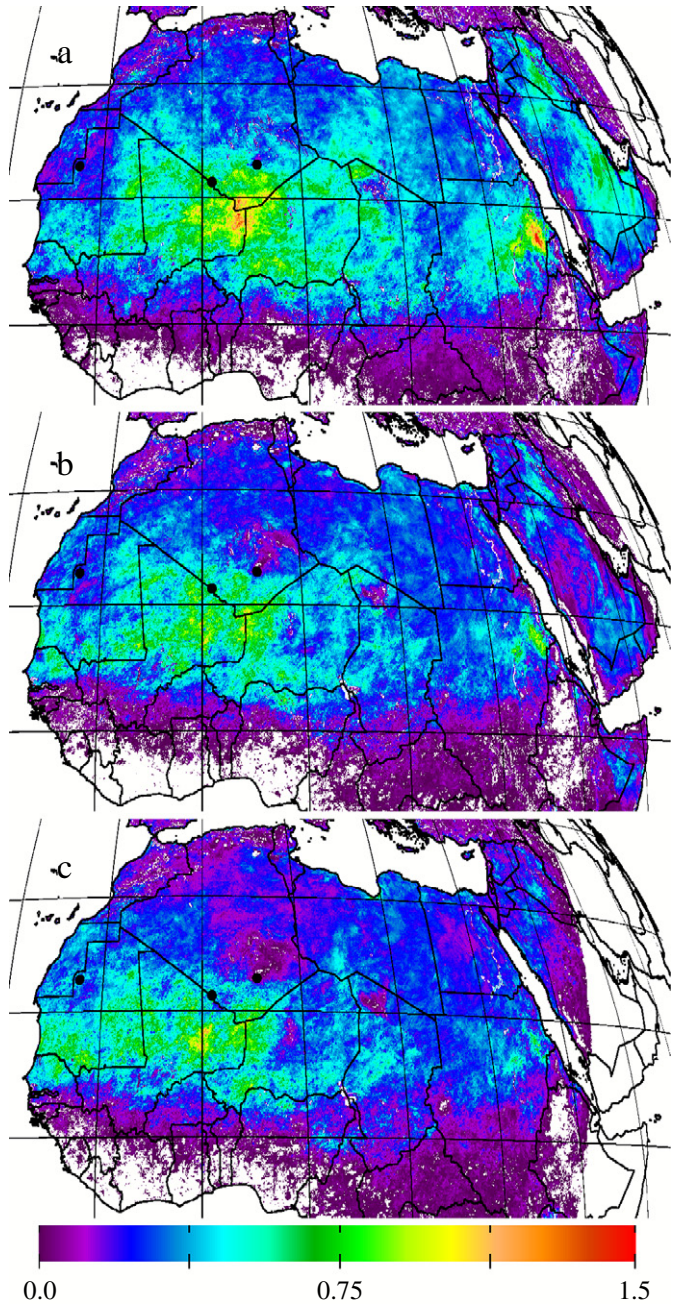


**Fig. 10.** Diurnal cycle of v2 monthly average DAOD for June 2009 at: (a) 1000 UT; (b) 1200 UT; (c) 1400 UT.

#### 4.1. Multi-year observations of DAOD: 2008–2010

Over a multi-year period we can build up a climatology of dust aerosol optical depth from SEVIRI and of aerosol optical depth from AERONET. Validation of the SEVIRI retrieval is presented over a three-year period in Fig. 12. From 2008 to 2010 AERONET data are available for nine of the eleven sites in Table 3. Observations from Bordj Badji Mokhtar and Zouerat (Zouerate-Fennec) start in 2011. Sites with large data gaps include Zinder Airport (which started routine observations in May 2009) and DMN Maine Soroa (which finished in July 2010) in Niger. Agreement between the SEVIRI DAOD and the dust-screened AERONET AOD is best at the central desert sites of Solar Village and Tamanrasset INM, with linear correlation values ( $v1/v2$ ) of 0.75/0.73 and 0.72/0.73, in areas of high dust loading.

**Table 3**

Latitudes and longitudes of relevant AERONET sites, with their associated viewing zenith angles with respect to SEVIRI, and the year of the last available Level 2 data (Level 1.5 data were used afterwards, when available).

Site name	Region	Lat. (°N)	Lon. (°E)	$\theta_v$ (°)	Level 2
Agoufou	Sahel	15.35	-1.48	18.0	2008
Banizoumbou	Sahel	13.54	2.67	16.2	2009
Bordj Badji Mokhtar	Sahara	21.33	0.95	25.0	No
DMN Maine Soroa	Sahel	13.22	12.02	20.9	2010
IER Cinzana	Sahel	13.28	-5.93	17.0	2009
Saada	Morocco	31.63	-8.16	37.8	2010
Sede Boker	Israel	30.86	34.78	52.0	2010
Solar Village	Arabia	24.91	46.40	58.7	2010
Tamanrasset INM	Sahara	22.79	5.53	27.4	No
Zinder Airport	Sahel	13.78	8.90	19.2	2009
Zouerate-Fennec	Sahara	22.75	-12.48	30.0	No

The contrast between the v1 and the v2 detections is not significant for most of the sites: most affected is Solar Village, near Riyadh in Saudi Arabia, close to the Jabal Tuwayq escarpment which gives rise to the arc of RSCFs in central Arabia. Over the three-year period the v2 detection removes 138 points, 1.9% of the v1 total (by comparison, the highest ratio for any other site is under 1%), but the effect on the correlation is still minor, reducing it by 0.02. There is no consistent pattern amongst the sites as to the effect of the v2 dust detection on the agreement with AERONET, so on the climatological time-scale we can argue that the effect of the RSCFs on the DAOD is minimal for these locations.

For comparison with BR09, statistics of linear correlations, RMS differences and biases (using daily average DAODs) for spring and summer 2008–2010 are detailed in Table 4. Note that BR09 used meteorological fields from ECMWF operational analyses, whereas this work uses the ERA-Interim reanalysis product. Tamanrasset INM and Zinder Airport were not used by BR09 since these sites were not operational in 2006, while Saada was excluded since the data were too sparse. At Solar Village the highest correlations are observed, as well as some of the lowest RMS differences and biases. Meanwhile at the four Sahel sites the correlations are generally reduced from the 2006 values, although at Agoufou the 2006 value is within the interannual variability for 2008–2010.

Over a longer, multi-annual timescale, we see reduced agreement between SEVIRI and AERONET than during spring and summer only (Table 5). There is a seasonal dependence at the Sahel sites: generally

in spring the agreement is best, reducing during the summer and into the autumn. At this time the Sahel is still within the dry season, but there is increased Saharan dust activity within the region. Analogously, at the central desert sites, the correlation is at a maximum in summer at the peak of Saharan activity, rising to 0.78 at Tamanrasset INM. At Sede Boker in Israel, one of the correlation peaks (0.61) is during spring when the Khamaseen wind (Abed et al., 2009) blows dust from the north-eastern Sahara across Egypt and the western Middle East. Hence it is apparent that the strongest correlations occur when the dust activity is at its peak, which varies by region.

The largest biases (Table 5) occur in winter at sites such as Tamanrasset INM and Saada, reaching a maximum value of 0.24. Analysis has shown that  $\Delta T_{B108}$  at these sites in winter is dominated by changes in meteorological conditions (variability in  $T_{B108\text{dfe}}$ ) rather than dust itself. Hence these biases may be reflecting the inability of either the retrieval scheme or the analysis fields to correctly capture the true variability.

#### 4.2. Fennec in June 2011 – Bordj Badji Mokhtar and Zouerat

During the Fennec field campaign in June 2011 (Washington et al., 2012), two new AERONET sites in the remote desert were established, at Bordj Badji Mokhtar (BBM) in the far south of Algeria (Marsham et al., submitted for publication), and Zouerat, in north-western Mauritania (the coordinates of these locations are detailed in Table 3). Before this effort only a very few AERONET sites had been placed in the central Sahara: two in the southern Algerian town of Tamanrasset, and one in the Bodélé Depression in Chad for several days in March 2005 during the BoDEx campaign (Todd et al., 2007; Washington et al., 2006). The new sites are located in a large area of the West African Sahara which has been identified as a major dust source region (e.g. (Engelstaedter et al., 2006; Washington et al., 2003)), especially during the summer (see also Fig. 2).

Observations from the Fennec AERONET stations in June 2011 are presented in Fig. 13, along with Tamanrasset INM, the other central Saharan site. The agreement between AERONET and SEVIRI is good, especially at higher dustloadings, typically seen during this month in the central Sahara at the Algerian sites. The differences between the v1 and v2 DAODs are small for these sites, effectively within noise, especially in June. Zouerat is much further west than the Algerian sites, is more susceptible to the influence of marine air coming in from the Atlantic, and is furthest away from the major source regions. Hence Zouerat

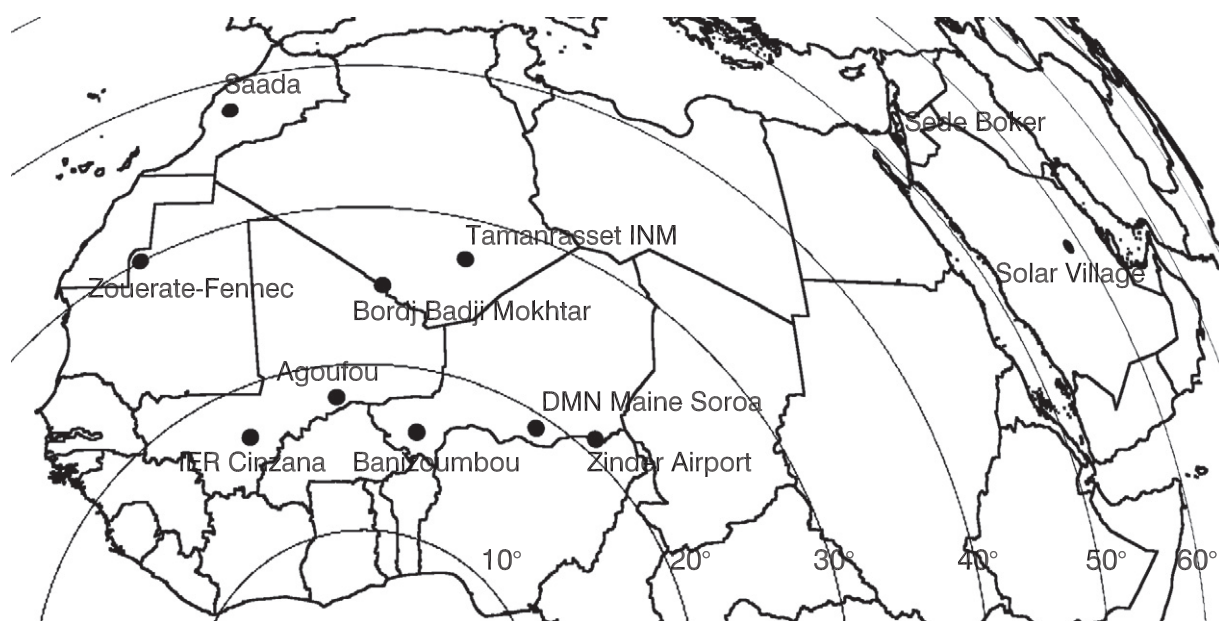
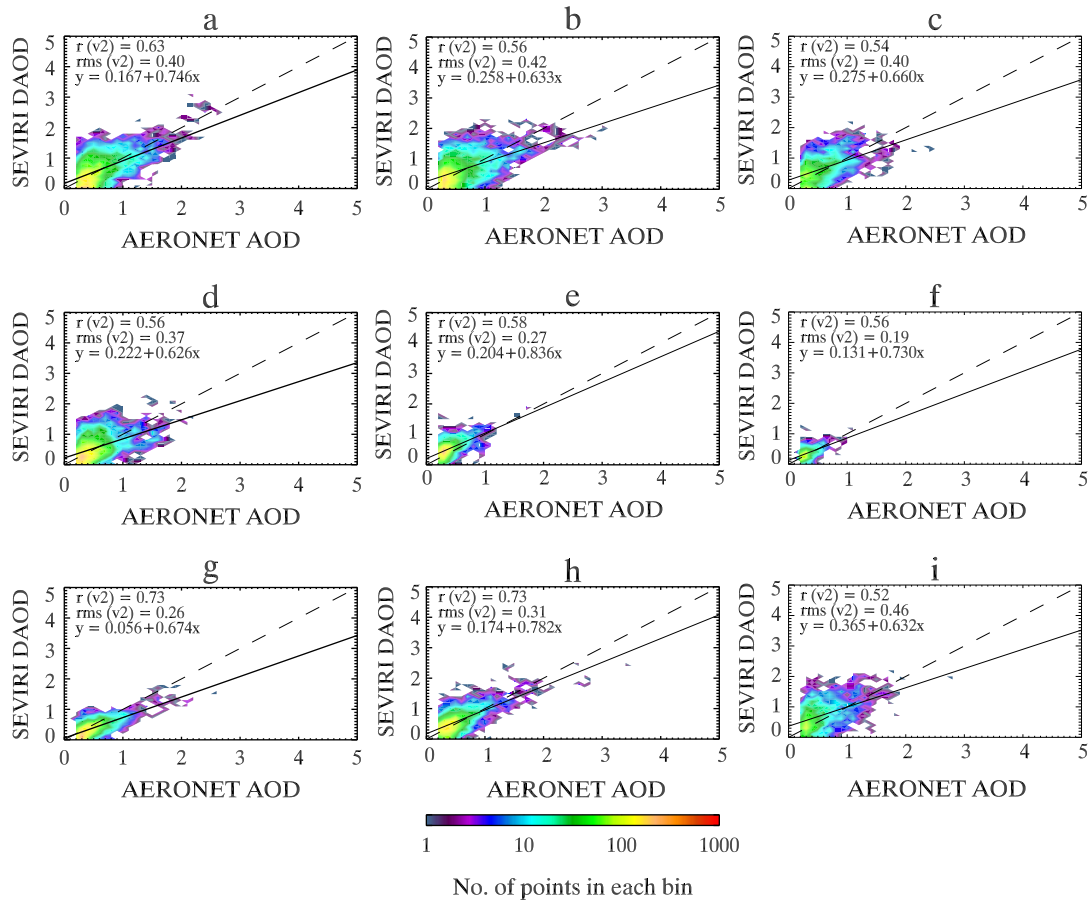


Fig. 11. Map of AERONET sites used in this study. Included are contour lines of the SEVIRI viewing zenith angles, at 10° spacings.



**Fig. 12.** Density histograms of coincident AERONET AOD and SEVIRI v2 DAOD measurements (at an AOD/DAOD resolution of 0.1), 2008–2010, over (a) Agoufou; (b) Banizoumbou; (c) DMN Maine Soroa; (d) IER Cinzana; (e) Saada; (f) Sede Boker; (g) Solar Village; (h) Tamanrasset INM; (i) Zinder Airport. Very little dust is seen below an AERONET AOD (at 550 nm) of ~0.2 due to the filtering for dust using  $\alpha$  and  $\tau_{1020 \text{ nm}}$ . The solid line indicates the best linear fit.

tends to see much lower dust loadings than do BBM and Tamanrasset. June 2011 saw several large dust events, including an event initially triggered by a convective system (over eastern Niger, and visible in the RGB imagery) late in the evening of the 16th which developed into a substantial dust storm over the triple-point of Mali, Niger and Algeria. On the 17th the storm was at its peak in the border areas, resulting in very high DAODs over BBM; over the following two days the system migrated north, passing over Tamanrasset on the 18th, so explaining the

lag in peak dust loadings between the two sites. AERONET and SEVIRI are in good agreement at both sites on both days. At BBM, the weather conditions can be divided into two distinct periods: before the 12th the atmospheric column was dry with little dust, and with a static bias between SEVIRI and AERONET. After the 13th there is a strong monsoon influence, bringing increased variability in the total column water vapour and higher dust and cloud cover (Marsham et al., submitted for publication), leading to a more variable bias in the retrievals.

## 5. Conclusions and discussion

An archive of dust detection and DAOD from MSG-SEVIRI has been built up over North Africa and the Middle East from January 2008 to the present, at a half-hourly temporal resolution during daylight hours. This has extended the time period presented in previous work (Brindley & Russell, 2009), which focused on spring and summer in one year (2006). Routine reprocessing has enabled us to study dust activity on a climatological timescale and during other seasons (winter and autumn), and has permitted more extensive validation of the dust products obtained from SEVIRI.

Winter dust detections have revealed substantial limitations in the original dust detection routine due to excessive generalisation in the dust detection thresholds. The method was designed over arid land surfaces, but was insufficiently discriminating between the wide variety of desert surfaces, varying between sandy dune fields, rocky hamadas, and hills and mountains. This led to surface features being misclassified as airborne dust, as evidenced by their static nature, their association with specific surface types and hence areas marked by specific combinations of surface emissivities, and the relative weakness of the SEVIRI

**Table 4**

Statistics of comparisons of daily averaged SEVIRI (v2) and AERONET data, documenting correlations, RMS differences, and biases (SEVIRI-AERONET), for spring and summer, with reference to values calculated by BR09 using data from March–August 2006. Ranges indicate the spread (minima/maxima) of the yearly statistics, for 2008–2010. Included are the values of AOD from AERONET over the coincident timeslots with SEVIRI data. BR09 did not use data from Saada, Tamanrasset INM, or Zinder Airport.

Site	Correlation	RMS	Bias	AOD
Agoufou	0.63/0.79	0.31/0.38	0.03/0.16	0.52/1.02
Banizoumbou	0.41/0.74	0.37/0.44	-0.05/0.16	0.56/0.95
DMN Maine Soroa	0.42/0.84	0.30/0.45	-0.04/0.22	0.49/0.85
IER Cinzana	0.53/0.81	0.36/0.41	-0.17/0.20	0.49/0.91
Sede Boker	0.60/0.73	0.13/0.17	0.02/0.09	0.18/0.26
Solar Village	0.77/0.93	0.14/0.29	-0.19/-0.06	0.39/0.60
<i>BR09</i>				
Agoufou	0.75	0.27	0.07	0.62
Banizoumbou	0.84	0.35	0.00	0.76
DMN Maine Soroa	0.88	0.35	0.12	0.77
IER Cinzana	0.81	0.30	0.08	0.62
Sede Boker	0.76	0.12	0.08	0.22
Solar Village	0.89	0.13	0.00	0.43

**Table 5**

Seasonal statistics of correlations, RMS differences and biases (SEVIRI-AERONET) of matched SEVIRI (v2) and AERONET data, 2008–2010 at half-hourly resolution, and the number of points. Included are the values of AOD from AERONET over the coincident timeslots with SEVIRI data.

Site	Region	All	Spring	Summer	Autumn	Winter
<i>Correlations</i>						
Agoufou	Sahel	0.63	0.65	0.65	0.49	0.26
Banizoumbou	Sahel	0.56	0.59	0.58	0.39	0.50
DMN Maine Soroa	Sahel	0.54	0.63	0.57	0.21	0.49
IER Cinzana	Sahel	0.56	0.62	0.58	0.33	0.43
Saada	Morocco	0.58	0.30	0.73	0.41	0.64
Sede Boker	Israel	0.56	0.61	0.38	0.66	0.14
Solar Village	Arabia	0.73	0.75	0.79	0.51	0.55
Tamanrasset INM	Sahara	0.73	0.67	0.78	0.46	0.52
Zinder Airport	Sahel	0.52	0.66	0.45	0.36	0.59
<i>RMS differences</i>						
Agoufou	Sahel	0.40	0.41	0.43	0.34	0.38
Banizoumbou	Sahel	0.42	0.44	0.45	0.39	0.38
DMN Maine Soroa	Sahel	0.40	0.38	0.43	0.43	0.38
IER Cinzana	Sahel	0.37	0.42	0.43	0.30	0.27
Saada	Morocco	0.27	0.31	0.22	0.38	0.39
Sede Boker	Israel	0.19	0.19	0.17	0.13	0.28
Solar Village	Arabia	0.26	0.27	0.27	0.18	0.22
Tamanrasset INM	Sahara	0.31	0.28	0.35	0.25	0.37
Zinder Airport	Sahel	0.46	0.45	0.48	0.48	0.39
<i>Biases</i>						
Agoufou	Sahel	0.00	0.04	0.06	-0.09	-0.04
Banizoumbou	Sahel	0.02	-0.04	0.19	-0.06	0.09
DMN Maine Soroa	Sahel	0.06	0.01	0.16	0.03	0.07
IER Cinzana	Sahel	0.00	-0.07	0.23	-0.04	-0.09
Saada	Morocco	0.13	0.10	0.13	0.19	0.24
Sede Boker	Israel	0.03	0.02	0.07	-0.01	0.08
Solar Village	Arabia	-0.12	-0.13	-0.17	-0.09	0.07
Tamanrasset INM	Sahara	0.04	0.00	0.10	0.02	0.20
Zinder Airport	Sahel	0.14	-0.06	0.20	0.20	0.18
<i>AERONET AOD</i>						
Agoufou	Sahel	0.68	0.72	0.80	0.54	0.58
Banizoumbou	Sahel	0.68	0.85	0.64	0.52	0.55
DMN Maine Soroa	Sahel	0.65	0.75	0.66	0.49	0.54
IER Cinzana	Sahel	0.62	0.76	0.63	0.50	0.50
Saada	Morocco	0.44	0.42	0.45	0.46	0.43
Sede Boker	Israel	0.40	0.45	0.34	0.33	0.38
Solar Village	Arabia	0.56	0.59	0.61	0.41	0.41
Tamanrasset INM	Sahara	0.58	0.58	0.69	0.43	0.47
Zinder Airport	Sahel	0.67	0.94	0.66	0.52	0.56
<i>No. of points</i>						
Agoufou	Sahel	7191	2146	2232	1979	834
Banizoumbou	Sahel	6832	2760	1358	1664	1050
DMN Maine Soroa	Sahel	3536	1359	1026	633	518
IER Cinzana	Sahel	6519	2226	1431	1703	1159
Saada	Morocco	2882	723	1781	241	137
Sede Boker	Israel	1103	559	209	220	115
Solar Village	Arabia	4015	1560	1598	515	342
Tamanrasset INM	Sahara	4644	1847	1703	956	137
Zinder Airport	Sahel	3169	743	1023	975	420

dust DAODs associated with these features. Two of the thresholds in the original scheme could be triggered by the surface. The more persistent feature is caused by high emissivity in the 8.7 μm channel, over vegetation or barren, rocky surfaces, frequently associated with lines of hills. The weaker feature is triggered by the reflectance component to the 3.9 μm thermal channel, and tends to occur where the 3.9 μm emissivity is lowest, frequently associated with sand seas. The 3.9 μm feature is most sensitive at high solar zenith angles when the albedo is highest (Wang et al., 2005). In addition, due to typically higher values of  $T_{B120} - T_{B108}$  when surface temperatures are colder, false detections were more frequently occurring in winter and at either end of the diurnal cycle. By eliminating dust detections when the difference between the brightness temperatures at 8.7 and 10.8 μm is within 2 K of the monthly average for a given period (Ashpole & Washington, 2012), we find that these

spurious dust detections are substantially reduced. This gives us greater confidence that the remaining detected 'dust' is in fact airborne dust.

Observations from AERONET do not provide significant evidence favouring either the v1 or the v2 dust detections, due to the limited spatial distribution of AERONET sites and their distance from the RSCFs. Rather, it is the evidence provided by the static nature of the features removed by the v2 detections, and case studies of their effect on the DAOD and the DAOD thresholds, which indicate the improvements brought in by the v2 detection. On the monthly averaged diurnal cycle, reduced dust detections are seen along the North African coast, where we would not expect to see persistent dust loading (Engelstaedter & Washington, 2007; Prospero et al., 2002), and where the 8.7 μm emissivity is high. What remains is amorphous, as would be expected of moving and dispersing atmospheric dust. There is also less dependence on the time-of-day. Case studies show dust from the v1 detection occurring where RGB imagery does not indicate dust presence.

The overall effect of the updated detection on the resultant DAOD is small, since our DAOD retrievals take place where there is no cloud, as well as where there is dust. Hence while the contrast between the v2 and the v1 dust detections may be very important when judging the dust flags, it does not appear to be a major consideration when judging the DAODs. Applying a consistent flag is however important. The new scheme gains a consistent threshold value of DAOD when the detection will be triggered of sim1.9 across the entire study region. The work here also shows the importance of implementing such a scheme, as otherwise high dust loadings, with potentially the largest influence on the instantaneous radiation fields, will be flagged as cloud.

DAOD comparisons with AERONET indicate that the DAOD retrieval algorithm is most reliable when the dust loadings are highest. In Israel this is during spring, while in the central Sahara this is during the summer. Sahel optical depths are highest in spring and summer (varying by site), although the summer DAOD retrievals may be an underestimate due to the increased cloud cover during the West African Monsoon, which may obscure heavy dust. In winter there is a higher bias of SEVIRI compared to AERONET AOD at sites such as Saada. At these sites very little dust is detected by AERONET in winter, and so the DAODs may be more affected by the variability in the meteorological conditions, specifically the skin temperature and the column moisture (C. Ansell, personal communication, 2012), than by the variability due to dust.

The new observations made at BBM and Zouerat as part of the Fennec project show the benefit of ground-based validation sites within regions of the highest dust loading. At the central Saharan sites the SEVIRI algorithm shows good agreement. Subsequent work will seek to assess space-based DAOD retrievals from alternative instruments and algorithms using the new AERONET observations.

## Acknowledgments

We thank colleagues at the Royal Meteorological Institute of Belgium for providing GERB and climatological reflectance data, and for extending the SEVIRI archive held at Imperial. Thanks also to ECMWF for producing the ERA-Interim data and to the British Atmospheric Data Centre (BADC) for providing access to the data. We also thank researchers at the Cooperative Institute for Meteorological Satellite Studies at the University of Wisconsin for the emissivity data, and the AERONET PIs and staff for establishing and maintaining the eleven sites used in this study. The Fennec supersites at BBM and Zouerat were operated by the Offices Nationals de la Météorologie (ONM) of Algeria and Mauritania. Thanks also to Richard Bantges, Claudio Belotti, Ken Bignell and Jon Murray at Imperial College, and John Marsham, Claire Ryder, Kerstin Schepanski and others from the Fennec consortium, for their useful comments during the preparation of this work. We thank two anonymous reviewers for their helpful feedback. This has been funded by the UK Natural Environment Research Council (under grant NE/G016283/1), within the framework of the Fennec project.

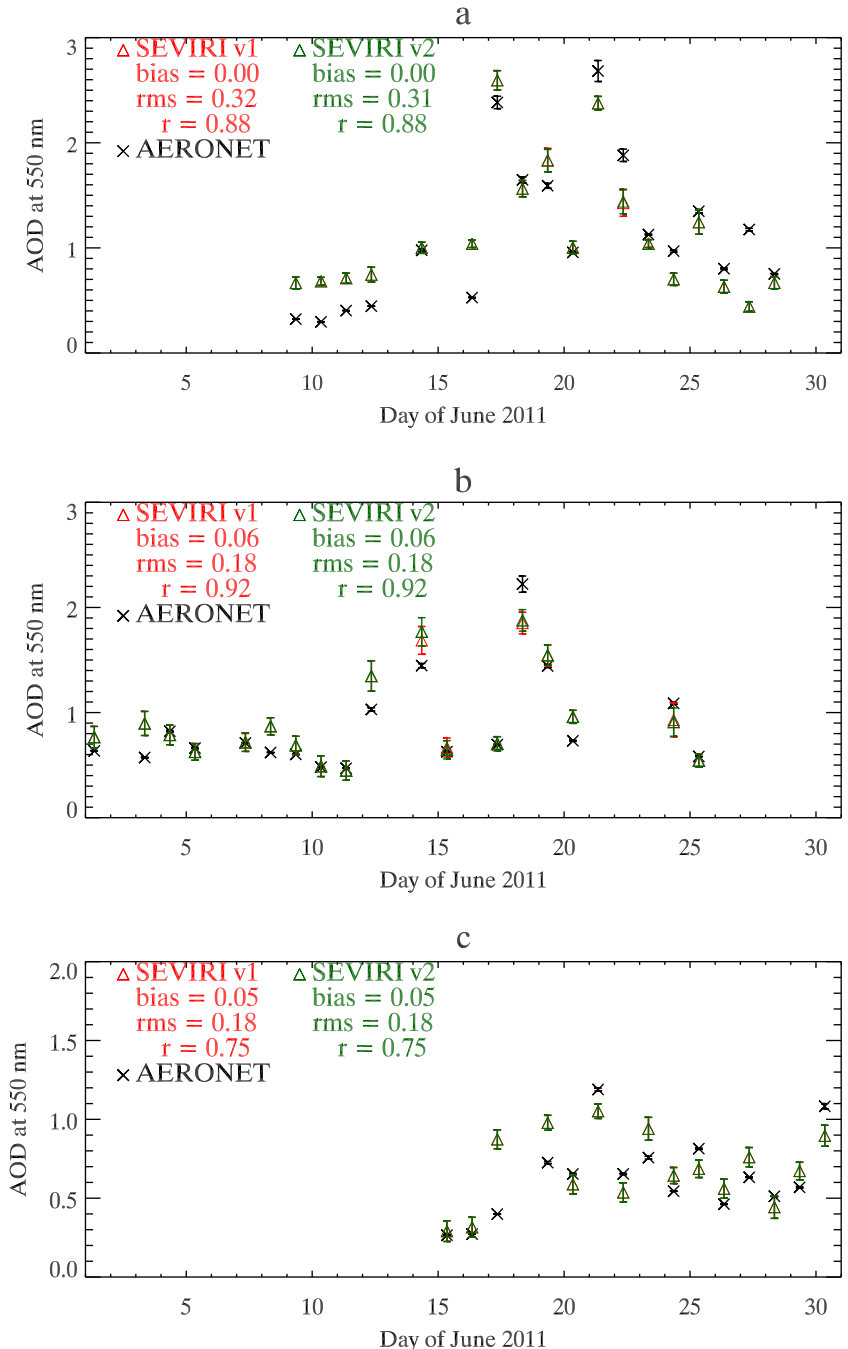


**Fig. 13.** Time-series of daily mean AOD from AERONET (black) and daily mean DAOD from SEVIRI v1 (red) and v2 (green) during June 2011 at (a) BBM, (b) Tamanrasset INM, and (c) Zouerat. Note the different AOD/DAOD scale at Zouerat. Error bars for AERONET are averaged errors from the available data for the day, while error bars for SEVIRI are derived from the standard deviation of the values of  $T_{B108}$  around each pixel: this value is then processed using the same method as for  $\Delta T_{B108}$  to find the uncertainty on the SEVIRI measurement.

## References

- Abed, A. M., Al-Kuisi, M., & Khair, H. A. (2009). Characterization of the Khamaseen (spring) dust in Jordan. *Atmospheric Environment*, 43, 2868–2876.
- Ackerman, S. A. (1989). Using the radiative temperature difference at 3.7 and 11 microns to track dust outbreaks. *Remote Sensing of Environment*, 27, 129–133.
- Ashpole, I., & Washington, R. (2012). An Automated dust detection using SEVIRI: A multi-year climatology of summertime dustiness in the central and Western Sahara. *Journal of Geophysical Research*, 117.
- Brindley, H. E. (2007). Estimating the top-of-atmosphere longwave radiative forcing due to Saharan dust from satellite observations over a West African surface site. *Atmospheric Science Letters*, 8, 74–79.
- Brindley, H. E., Knippertz, P., Ryder, C., & Ashpole, I. (2012). A critical evaluation of the ability of the Spinning Enhanced Visible and InfraRed Imager (SEVIRI) thermal infrared red-green-blue rendering to identify dust events: Theoretical analysis. *Journal of Geophysical Research*, 117.
- Brindley, H. E., & Russell, J. E. (2009). An assessment of Saharan dust loading and the corresponding cloud-free longwave direct radiative effect from geostationary satellite observations. *Journal of Geophysical Research*, 114.
- Dee, D. P., Uppala, S. M., Simmons, A. J., Berrisford, P., Poli, P., Kobayashi, S., et al. (2011). The ERA-Interim reanalysis: Configuration and performance of the data assimilation system. *Quarterly Journal of the Royal Meteorological Society*, 137, 553–597.
- Derrien, M., & Le Gléau, H. (2005). MSG/SEVIRI cloud mask and type from SAFNWC. *International Journal of Remote Sensing*, 26, 4707–4732.
- Dubovik, O., Holben, B., Eck, T. F., Smirnov, A., Kaufman, Y. J., King, M. D., et al. (2002). Variability of absorption and optical properties of key aerosol types observed in worldwide locations. *Journal of the Atmospheric Sciences*, 59, 590–608.

- Eck, T. F., Holben, B. N., Reid, J. S., Dubovik, O., Smirnov, A., O'Neill, N. T., et al. (1999). Wavelength dependence of the optical depth of biomass burning, urban, and desert dust aerosols. *Journal of Geophysical Research*, 104, 333–349.
- Engelstaedter, S., Tegen, I., & Washington, R. (2006). North African dust emissions and transport. *Earth-Science Reviews*, 79, 73–100.
- Engelstaedter, S., & Washington, R. (2007). Atmospheric controls on the annual cycle of North African dust. *Journal of Geophysical Research*, 112.
- Evan, A. T., Heidinger, A. K., & Pavolonis, M. J. (2006). Development of a new overwater advanced very high resolution radiometer dust detection algorithm. *International Journal of Remote Sensing*, 27, 3903–3924.
- Forster, P., Ramaswamy, V., Artaxo, P., Bernsten, T., Betts, R., Fahey, D. W., et al. (2007). *Changes in atmospheric constituents and in radiative forcing*. Cambridge, United Kingdom and New York, NY, USA: Cambridge University Press (chapter 2).
- Ginoux, P., Garbuзов, D., & Hsu, N. C. (2010). Identification of anthropogenic and natural dust sources using Moderate Resolution Imaging Spectroradiometer (MODIS) Deep Blue level 2 data. *Journal of Geophysical Research*, 115.
- Ginoux, P., Prospero, J. M., Torres, O., & Chin, M. (2004). Long-term simulation of global dust distribution with the GOCART model: Correlation with North Atlantic Oscillation. *Environmental Modelling and Software*, 19, 113–128.
- Goudie, A. S., & Middleton, N. J. (2006). *Desert dust in the global system*. Heidelberg, Germany: Springer.
- Guerroni, S., Molinaroli, E., & Chester, R. (1997). Saharan dust inputs to the western Mediterranean Sea: Depositional patterns, geochemistry and sedimentological implications. *Deep-Sea Research II*, 44, 631–654.
- Harries, J. E., Russell, J. E., Hanafin, J. A., Brindley, H., Futyan, J., Rufus, J., et al. (2005). The geostationary earth radiation budget project. *Bulletin of the American Meteorological Society*, 86, 945–960.
- Haywood, J. M., Johnson, B. T., Osborne, S. R., Baran, A. J., Brooks, M., Milton, S. F., et al. (2011). Motivation, rationale and key results from the GERBILS Saharan dust measurement campaign. *Quarterly Journal of the Royal Meteorological Society*, 137, 1106–1116.
- Heidinger, A. K., Frey, R., & Pavolonis, M. (2004). Relative merits of the 1.6 and 3.75 micron channels of the AVHRR/3 for cloud detection. *Canadian Journal of Remote Sensing*, 30, 182–194.
- Holben, B. N., Eck, T. F., Slutsker, I., Tanré, D., Buis, J. P., Setzer, A., et al. (1998). AERONET – A federated instrument network and data archive for aerosol characterization. *Remote Sensing of Environment*, 66, 1–16.
- Hsu, N. C., Herman, J. R., & Weaver, C. (2000). Determination of radiative forcing of Saharan dust using combined TOMS and ERBE data. *Journal of Geophysical Research*, 105, 20,649–20,661.
- Ipe, A., Bertrand, C., Clerbaux, N., Dewitte, S., & Gonzalez, L. (2004). Validation and homogenization of cloud optical depth and cloud fraction retrievals for GERB/SEVIRI scene identification using Meteosat-7 data. *Atmospheric Research*, 72, 17–37.
- Jickells, T. D., An, Z. S., Andersen, K. K., Baker, A. R., Bergametti, G., Brooks, N., et al. (2005). Global iron connections between desert dust, ocean biogeochemistry, and climate. *Science*, 308, 67–71.
- Jin, M., & Liang, S. (2006). An improved land surface emissivity parameter for land surface models using global remote sensing observations. *Journal of Climate*, 19, 2867–2881.
- Klaver, A., Formenti, P., Caquineau, S., Chevaillier, S., Ausset, P., Calzolai, G., et al. (2011). Physico-chemical and optical properties of Sahelian and Saharan mineral dust: in situ measurements during the GERBILS campaign. *Quarterly Journal of the Royal Meteorological Society*, 137, 1193–1210.
- Lensky, I. M., & Rosenfeld, D. (2008). Clouds-aerosols-precipitation satellite analysis tool (CAPSAT). *Atmospheric Chemistry and Physics*, 8, 6739–6753.
- Liu, D., Wang, Z., Liu, Z., Winker, D., & Trepte, C. (2008). A height resolved global view of dust aerosols from the first year CALIPSO lidar measurements. *Journal of Geophysical Research*, 113.
- Mabbutt, J. A. (1977). *Desert landforms*. Cambridge, Massachusetts: The MIT Press.
- Marsham, J. H., Hobby, M., Allen, C. J. T., Banks, J. R., Bart, M., Brooks, B., Cazavos-Guerra, C., Engelstaedter, S., Gasgoyne, M., Lima, A., Martins, V., McQuaid, J. B., O'Leary, A., Ouchene, B., Ouladichir, A., Parker, D. J., Saci, A., Salah-Ferroudj, M., Todd, M. C., & Washington, R. (submitted for publication). Meteorology and dust in the central Sahara: Observations from Fennec supersite-1 during the June 2011 Intensive Observation Period.
- Marsham, J. H., Knippertz, P., Dixon, N. S., Parker, D. J., & Lister, G. M. S. (2011). The importance of the representation of deep convection for modeled dust generating winds over West Africa during summer. *Geophysical Research Letters*, 38.
- Martonchik, J. V., Diner, D. J., Kahn, R., Gaitley, B., & Holben, B. N. (2004). Comparison of MISR and AERONET aerosol optical depths over desert sites. *Geophysical Research Letters*, 31.
- Merchant, C., Embury, O., Borgne, P. L., & Bellec, B. (2006). Saharan dust in nighttime thermal imagery: Detection and reduction of related biases in retrieved sea surface temperature. *Remote Sensing of Environment*, 104, 15–30.
- MétéoFrance (2011). *Algorithm theoretical basis document for cloud products (CMa-PGE01 v3.2, CT-PGE02 v2.2 & CTH-PGE03 v2.2)*. Technical Report SAF/NWC/CDOP/MFL/SCI/ATBD/01. Paris: MétéoFrance.
- Miller, S. D. (2003). A consolidated technique for enhancing desert dust storms with MODIS. *Geophysical Research Letters*, 30.
- Prata, A. J. (1989). Observations of volcanic ash clouds in the 10–12 micron window using AVHRR/2 data. *International Journal of Remote Sensing*, 10, 751–761.
- Prospero, J. M., Ginoux, P., Torres, O., Nicholson, S. E., & Gill, T. E. (2002). Environmental characteristics of global sources of atmospheric soil dust identified with the Nimbus 7 Total Ozone Mapping Spectrometer (TOMS) Absorbing Aerosol Product. *Reviews of Geophysics*, 40.
- Redelsperger, J.-L., Thorncroft, C. D., Diedhiou, A., Lebel, T., Parker, D. J., & Polcher, J. (2006). African monsoon multidisciplinary analysis: An international research project and field campaign. *Bulletin of the American Meteorological Society*, 87, 1739–1746.
- Schepanski, K., Tegen, I., Laurent, B., Heinold, B., & Macke, A. (2007). A new Saharan dust source activation frequency map derived from MSG-SEVIRI IR-channels. *Geophysical Research Letters*, 34.
- Schepanski, K., Tegen, I., Todd, M. C., Heinold, B., Bönisch, G., Laurent, B., et al. (2009). Meteorological processes forcing Saharan dust emission inferred from MSG-SEVIRI observations of subdaily dust source activation and numerical models. *Journal of Geophysical Research*, 114.
- Schmetz, J., Pili, P., Tjemkens, S., Just, D., Kerkemann, J., Rota, S., et al. (2002). An introduction to meteosat second generation (MSG). *Bulletin of the American Meteorological Society*, 83, 977–992.
- Seemann, S. W., Borbas, E. E., Knuteson, R. O., Stephenson, G. R., & Huang, H.-L. (2008). Development of a global infrared land surface emissivity database for application to clear sky sounding retrievals from multispectral satellite radiance measurements. *Journal of Applied Meteorology and Climatology*, 47, 108–123.
- Slingo, A., Ackerman, T. P., Allan, R. P., Kassianov, E. I., McFarlane, S. A., Robinson, G. J., et al. (2006). Observations of the impact of a major Saharan dust storm on the atmospheric radiation balance. *Geophysical Research Letters*, 33.
- Tier, P., Feichter, J., Kinne, S., Kloster, S., Vignati, E., Wilson, J., et al. (2005). The aerosol-climate model ECHAM5-HAM. *Atmospheric Chemistry and Physics*, 5, 1125–1156.
- Todd, M. C., Washington, R., Martins, J. V., Dubovik, O., Lizcano, G., M'Bainayel, S., et al. (2007). Mineral dust emission from the Bodélé Depression, northern Chad, during BoDEx 2005. *Journal of Geophysical Research*, 112.
- Torres, O., Bhartia, P. K., Herman, J. R., Sinyuk, A., Ginoux, P., & Holben, B. (2002). A long-term record of aerosol optical depth from TOMS observations and comparison to AERONET measurements. *Journal of the Atmospheric Sciences*, 59, 398–413.
- Wang, Z., Barlage, M., Zeng, X., Dickinson, R. E., & Schaaf, C. B. (2005). The solar zenith angle dependence of desert albedo. *Geophysical Research Letters*, 32.
- Washington, R., Parker, D. J., Marsham, J. H., McQuaid, J., Brindley, H., Todd, M. C., Highwood, E. J., Flamant, C., Chaboureau, J.-P., Kocha, C., Saci, A., & Bechir, M. (2012). Fennec – The Saharan Climate System (part of the AMMA legacy). Presented at the 4th International AMMA Conference, Toulouse, July 2012. URL: [http://amma-conf2012.ipsl.fr/data/documents/PL1\\_3WashingtonLR.pdf](http://amma-conf2012.ipsl.fr/data/documents/PL1_3WashingtonLR.pdf)
- Washington, R., Todd, M. C., Engelstaedter, S., Mbainayel, S., & Mitchell, F. (2006). Dust and the low-level circulation over the Bodélé Depression, Chad: Observations from BoDEx 2005. *Journal of Geophysical Research*, 111.
- Washington, R., Todd, M., Middleton, N. J., & Goudie, A. S. (2003). Dust-storm source areas determined by the total ozone monitoring spectrometer and surface observations. *Annals of the Association of American Geographers*, 93, 297–313.
- Winker, D. M., Vaughan, M. A., Omar, A. H., Hu, Y., & Powell, K. A. (2009). Overview of the CALIPSO mission and CALIOP data processing algorithms. *Journal of Atmospheric and Oceanic Technology*, 26, 2310–2323.